A study of the origin of a quantum advantage in simulated annealing

Master Thesis

Author:
Elias Andre Starchl

Supervisor:
Univ. Prof. Dr. Helmut Ritsch

Institute for Theoretical Physics
University of Innsbruck
Austria

October 6, 2020

Abstract

Simulated quantum annealing is a well method for finding solutions to classical or quantum optimization problems, which can be encoded in the ground state properties of a many-body Hamiltonian. Its central idea is to implement a quantum system with a time dependent Hamiltonian slowly changing from a simple initial Hamiltonian to the desired target Hamiltonian. For a suitable timing this allows to let the ground state of the initial Hamiltonian evolve into the ground state of the final target Hamiltonian, which then allows to extract the solution to the optimization problem. It has been argued that under suitable conditions such a quantum implementation scales superior to a classical implementation based on thermal diffusion and slow cooling. Here we present a generic case, where both, a classical and a quantum description of the dynamics can be applied and directly compared by numerical simulations.

As generic example we study a small Bose-Hubbard type system describing particles inside a cavity generated optical lattice. Specifically, as minimal nontrivial instance we look at two atoms inside the cavity, confined by an external trapping potential and directly pumped by two laser beams inducing photon scattering into two separate cavity modes. Introducing an additional local energy shift at a specific lattice site allows to create a unique energy separated optimal ground state for the problem Hamiltonian. The main focus is to compare the full quantum mechanical model to the semi-classical model, where the field modes implementing interactions are approximated by classical coherent fields.

Essentially, our investigation reveals strong differences between the quantum and semi-classical model, which can be cast into a sort of phase diagram separating a distinct parameter region where quantum annealing does not find the optimum in the semi-classical approach but full quantum annealing does. We find strong evidence for the involvement of entanglement for finding an optimal solution and its influence on the minimal time needed for a successful simulation.

As an extra direction we study the impact of different photon number cut-offs in the numerical quantum simulation. Most surprisingly we find even an improvement in the optimization success rate for short simulation times, when we use too low cut-off numbers to get a numerically accurate solution of the Schrödinger equation. Using higher cut-off numbers and thus a better representation of the exact quantum dynamics seems to be more relevant only for longer simulation times with very high success rates. Again this appears to be related to the entanglement entropy of the system. All results are generated by numerical simulations using the QuantumOptics Framework for the Julia language locally developed in Innsbruck [31].

Zusammenfassung

Simuliertes quantum annealing ist eine gute Methode, um Lösungen für klassische- oder quanten-Optimierungsprobleme zu finden, welche in den Grundzustandseigenschaften eines Viel-Teilchen Hamiltonians kodiert werden können. Die Zentrale Idee ist ein Quantensystem zu implementieren, mit einem zeitabhängigen Hamiltonian, welcher langsam von einem simplen Anfangs-Hamiltonian zu einem Ziel-Hamiltonian wechselt. Für eine geeignete Zeit erlaubt dies den Grundzustand des Anfangs-Hamiltonian zu dem Grundzustand des finalen Ziel-Hamiltonian zu entwickeln, was dann die Entnahme der Lösung zu dem Optimierungsproblem erlaubt. Es wurde argumentiert, dass unter geeigneten Bedingungen eine solche Quantenimplementierung besser skaliert als eine klassische Implementierung, basierend auf thermaler Diffusion und langsamen kühlen. Hier präsentieren wir einen allgemeinen Fall, in welchem beide, eine klassische und eine Quanten-Beschreibung der Dynamik, eingesetzt und direkt durch numerische Simulationen verglichen werden können.

Als allgemeines Beispiel untersuchen wir ein kleines Bose-Hubbard-artiges System, welches Teilchen in einem Resonator generierten optischen Gitter beschreibt. Besonders, als kleinster nicht trivialer Fall, schauen wir uns zwei Atome in einem Resonator an, gefangen von einem externen Fang-Potential und direkt gepumpt durch zwei Laserstrahlen, welche Streuung in zwei separate Resonator-Moden erzeugen. Die Einführung einer zusätzlichen lokalen Energieverschiebung an einem bestimmten Gitterplatz erlaubt es einen eindeutigen, Energie-separierten, optimalen Grundzustand des Problem- Hamiltonian zu erzeugen. Der Hauptfokus ist es das komplette quanten Modell mit dem semi-klassischen Modell zu vergleichen, bei welchem die Feldmoden, welche Interaktionen erzeugen, durch klassische kohärente Felder angenähert werden.

Im Grunde zeigt unsere Untersuchung starke Unterschiede zwischen dem quanten und dem semi-klassischen Modell, welche in der Form ähnlich einem Phasendiagramm dargestellt werden können, einen bestimmten Parameterbereich separierend, wo quantum annealing kein Optimum für das semiklassischen Vorgehen erbringt aber das volle quantum annealing schon. Wir finden starke Beweise für das Mitwirken von Quantenverschränkung beim Finden einer optimalen Lösung und ihre Influenz auf die minimale Zeit, die benötigt wird für eine erfolgreiche Simulation.

Zusätzlich untersuchen wir die Auswirkung von unterschiedlichen Photonen-Zahl cut-offs in der numerischen quanten Simulation. Sehr überraschend finden wir sogar eine Verbesserung in der Optimierungs-Erfolgs-Rate für kurze Simulationszeiten, wenn wir für eine numerisch akkurate Lösung der Schrödinger Gleichung eine zu niedrige cut-off Zahlen verwenden. Verwenden einer höheren cut-off Zahl und damit eine bessere Repräsentation der exakten Quantendynamik scheint nur für längere Simulationszeiten mir sehr hoher Erfolgsrate relevant zu sein. Es scheint, dass dies ebenso mit der Verschränkungs-Entropie des Systems zusammenhängt. Alle Resultate wurden durch numerische Simulationen generiert, unter der Benutzung des QuantumOptics Frameworks für die Julia Programmiersprache, lokal entwickelt in Innsbruck [31].

Danksagung

Zunächst möchte ich mich an dieser Stelle vor allem bei meinen Eltern und meinem Bruder herzlich für die stetige Unterstützung bedanken. Ohne sie wäre mein Studium nicht möglich gewesen.

Einen besonderen Dank gebührt auch Herrn Prof. Ritsch für seine sowohl fachlich als auch menschlich herausragende Betreuung und Leitung während meiner ganzen Masterarbeit.

Außerdem möchte ich meinen Dank an alle Mitglieder der Arbeitsgruppe aussprechen, die mich freundlich aufgenommen haben, und immer für Fragen offen waren. Insbesondere möchte ich David Plankensteiner danken, der mir bei allen technischen Fragen zur Seite stand.

Abschließend möchte ich mich auch noch vor allem bei meinen Freunden bedanken. Ohne ihre Hilfe und Verständnis in jeglicher schwierigen Situation wäre vieles nicht möglich gewesen.

Contents

Chapter 1

Introduction

The idea of quantum computation (QC) has been around since 1980, when Paul Benioff first proposed a quantum Turing machine [6] and Feynman introduced the universal quantum simulator [18]. Shortly after, David Deutsch introduced the universal quantum computer in terms of the circuit model [12]. Nowadays, the journey towards an universal quantum computer has made immense progress, drawing interest from huge tech companies like Google and IBM and also universities from all over the world. Using quantum degrees of freedom to simulate physical problems was, and still is, an innovative and promising idea, giving rise to a huge new field of fundamental and applied sciences and is the leading aim of the second quantum revolution [15].

One of the many motivations behind all developments in quantum computation is the aim to study the complex mechanisms of quantum systems, which are extremely hard to observe in a laboratory and are intractable for classical modern supercomputers. Although universal quantum computers are proven to run some quantum algorithms exponentially faster then their classical equivalents, it is clear by now, that large scale quantum computers with functioning error correction are extremely hard to realize [39]. Consequently it opened the door to the research of less demanding options like adiabatic quantum optimization and quantum annealing.

In adiabatic quantum computation the simulation starts with an initial Hamiltonian for which the ground state is easy to prepare. One then slowly changes the Hamiltonian, proceeding to the ground state of a final Hamiltonian which encodes the solution to an optimization problem of interest. This encoding of a problem in a Hamiltonian started as quantum stochastic optimization [2] to solve classical optimization problems and later was renamed

quantum annealing (QA) [3]. Here instead of minimizing a certain function, one minimizes the energy of a state for a given Hamiltonian. The theoretical foundation for this to work is given by the adiabatic theorem [7] which in essence expresses the fact that a system will remain in the ground state or any other energy eigenstate if the Hamiltonian is changed slowly and the energy gap from the ground to excited states is big enough to suppress the transition to higher energy levels.

In contrast to the full scale quantum computers, this kind of protocol can already be implemented in simpler setups like quantum simulators. They have been realized in different forms, e.g. trapped-ion simulators [10], superconducting qubits [11] or ultra cold atoms in optical lattices [27]. Also commercially available superconducting quantum annealing devices exist since 2011 in the form of the D-Wave quantum annealer [25].

It is not yet clear if these quantum annealing devices offer an actual speedup over classical devices [21]. A hint for a probable advantage of quantum annealing is given in [42], where quantum annealing is used to solve a N-queens optimization problem [32]. In the paper it is suggested that a solution to the problem can only be found by using a full quantum description. The semi-classical mean-field approach for the cavity field fails to find a correct pattern for solving the problem. In this thesis we will use a similar but simplified model to investigate the advantage over the semi-classical field approximation, by using a full quantum description.

In a semi-classical model we replace the field operator of a field mode (=harmonic oscillation) by its expectation value, i.e. c-number. Considering a one-dimensional optical lattice in a cavity with two additional modes we show that the semi-classical approach fails to find the correct solution to our optimization problem for a specific range of parameters. In contrast to that the full quantum approach will be shown to be very reliable in finding the correct solution. Therefore, we thoroughly study the system and try to develop a feasible explanation for the behavior.

This thesis is organized as follows. Chapter 2 will introduce the theoretical background. In section 2.1.1, we first derive and then modify a Bose-Hubbard type Hamiltonian. Then we introduce the basic concepts of quantum annealing in section 2.2 and give a simple description of the adiabatic approximation. We talk about the general concept of self-organization in optical systems in section 2.3.The next chapter 3.1 is about analyzing the system in the full quantum description. This will be followed by a comparison to the semi-classical mean-field description 3.2. Finally we will discuss

the numerical photon cut-off and the impact on the quality of the solution in sect 3.2.2.

Chapter 2

Theoretical concepts

2.1 The model

In this chapter we will introduce the physical model system that will be used in this thesis. The idea is to use an as simple as possible system, which allows to identify a quantum advantage using atoms in an optical lattice within a cavity. We use a one dimensional lattice, with only four sites and periodic boundary conditions inside a cavity, filled with two particles. Non local interactions are mediated by two cavity modes.
In the following we will at first derive the general-Bose-Hubbard type Hamiltonian as described in [37]. Then we will adjust the Hamiltonian to fit our model and assumptions of two particles in 4 wells generated by two laser modes. Also the required approximations for the system will be explained. Finally the field eliminated Hamiltonian and the mean-field approximation with classical fields will be introduced.

2.1.1 Derivation of the Bose-Hubbard type Hamiltonian

Following [37], we first derive a general Bose-Hubbard type Hamiltonian. We consider N two level atoms in a cavity interacting with a standing wave cavity mode. This system is schematically shown in figure 2.1 and can be described by the Jaynes-Cummings Hamiltonian, consisting of three parts [24]

$$H_{JC} = H_A + H_R + H_{Int}. \tag{2.1}$$

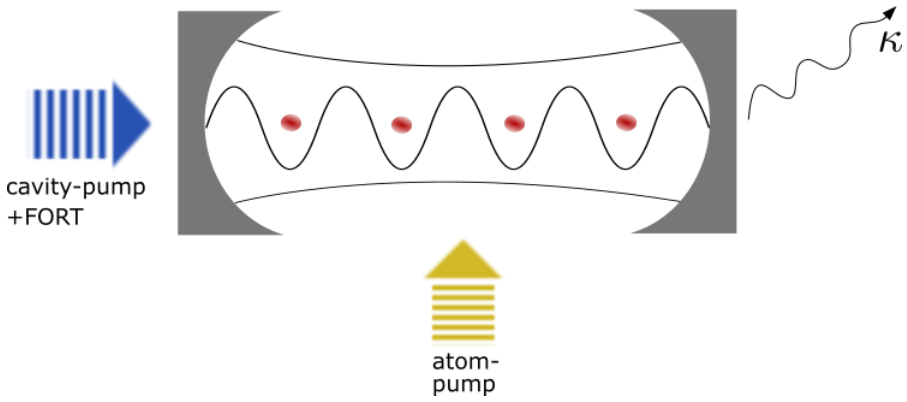

Figure 2.1: A schematic picture of the system for the Bose-Hubbard Hamiltonian. Shown is the cavity with particles inside an optical lattice. Direct atom pumping, pumping through the cavity mirrors and a far off resonant dipole trap (FORT) are depicted. The loss of photons through the cavity mirror is denoted by κ.

The three terms refer to the Hamiltonian of the atoms, the radiation field inside the cavity and the atom-field interaction respectively. They assume the form

$$H_A = \frac{\hat{p}^2}{2m} + V_e(x)\sigma^+\sigma^- + V_g(x)\sigma^-\sigma^+ + \hbar\omega_{eg}\sigma^+\sigma^- \tag{2.2}$$
$$- i\hbar h(x)(\sigma^+ e^{-i\omega_p t} - \sigma^- e^{i\omega_p t}),$$
$$H_R = \hbar\omega_c a^\dagger a - i\hbar\eta(a e^{i\omega_p t} - a^\dagger e^{-i\omega_p t}), \tag{2.3}$$
$$H_{Int} = -i\hbar g(x)(\sigma^+ a - \sigma^- a^\dagger). \tag{2.4}$$

Where we considered atoms of mass m and transition frequency ω_{eg}. The lowering and raising operator of the atomic excitation are given by σ^- and σ^+, respectively. The pump-field frequency is given by ω_p and the corresponding mode-function by $h(x)$. The same holds for the cavity fields with frequency ω_c and mode-function $g(x)$ and a describing the annihilation of a cavity photon. $V_e(x)$ and $V_g(x)$ are external trapping potentials only acting on atoms in the excited or ground state, respectively. Finally we have the pump-field amplitude η and the momentum operator of the atoms $\hat{p}$.

First we eliminate the explicit time-dependence by applying the unitary transformation $U(t) = \exp\left[i\omega_p t(\sigma^+\sigma^- + a^\dagger a)\right]$ and neglecting the fast rotating terms, known as the rotating wave approximation. After introducing

$\Delta_c = \omega_p - \omega_c$ and $\Delta_a = \omega_p - \omega_{eg}$ as the pump-cavity and pump-atom detuning, equations (2.2) can be written as

$$\begin{aligned} H_A =& \frac{\hat{p}^2}{2m} + V_e(x)\sigma^+\sigma^- + V_g(x)\sigma^-\sigma^+ + \hbar\Delta_a\sigma^+\sigma^- \\ & - i\hbar h(x)(\sigma^+ - \sigma^-), \end{aligned} \tag{2.5}$$

$$H_R = -\hbar\Delta_c a^\dagger a - i\hbar\eta(a - a^\dagger), \tag{2.6}$$

$$H_{Int} = -i\hbar g(x)(\sigma^+ a - \sigma^- a^\dagger). \tag{2.7}$$

The next step is to change to a many-body formalism in the second quantization formalism [41]. The atomic Hamiltonian then reads:

$$\begin{aligned} H_A = \int d^3\boldsymbol{x} \big[& \Psi_g^\dagger(\boldsymbol{x}) \big(-\frac{\hbar^2}{2m}\nabla^2 + V_g(\boldsymbol{x}) \big) \Psi_g(\boldsymbol{x}) \\ & + \Psi_e^\dagger(\boldsymbol{x}) \big(-\frac{\hbar^2}{2m}\nabla^2 - \hbar\Delta_a + V_e(\boldsymbol{x}) \big) \Psi_e(\boldsymbol{x}) \big], \end{aligned} \tag{2.8}$$

where we used the atomic field operators $\Psi_g(\boldsymbol{x})$ and $\Psi_e(\boldsymbol{x})$ for creating an atom at position $\boldsymbol{x}$ in the ground state or excited state, respectively. They obey the bosonic commutation relations

$$\big[\Psi_i(\boldsymbol{x}), \Psi_j^\dagger(\boldsymbol{x}')\big] = \delta^3(\boldsymbol{x} - \boldsymbol{x}')\delta_{i,j} \tag{2.9}$$

$$\big[\Psi_i(\boldsymbol{x}), \Psi_j(\boldsymbol{x}')\big] = \big[\Psi_i^\dagger(\boldsymbol{x}), \Psi_j^\dagger(\boldsymbol{x}')\big] = 0, \tag{2.10}$$

for $i, j \in \{e, g\}$. There is no change to H_R since it only depends on the photon fields and not on atomic operators.
Next we include particle-particle interactions via a short-range pseudo-potential, dominated by the s-wave scattering channel and therefore fully described by the scattering-length a_s. Leading to an interaction Hamiltonian

$$H_{A-A} = \frac{U}{2} \int d^3\boldsymbol{x} \Psi_g^\dagger(\boldsymbol{x})\Psi_g^\dagger(\boldsymbol{x})\Psi_g(\boldsymbol{x})\Psi_g(\boldsymbol{x}), \tag{2.11}$$

with the interaction Parameter $U = 4\pi a_s\hbar^2/m$ [22]. Finally we can describe the atom interaction with the cavity fields H_{A-R} and the pump fields H_{A-P} by

$$H_{A-R} = -i\hbar \int d^3\boldsymbol{x} \Psi_g^\dagger(\boldsymbol{x}) g(\boldsymbol{x}) a^\dagger \Psi_e(\boldsymbol{x}) + h.c., \tag{2.12}$$

$$H_{A-P} = -i\hbar \int d^3\boldsymbol{x} \Psi_g^\dagger(\boldsymbol{x}) h(\boldsymbol{x}) \Psi_e(\boldsymbol{x}) + h.c.. \tag{2.13}$$

where $h.c.$ denotes the hermitian conjugate.

As we are interested in the low temperature regime and want to ensure weak atomic excitation, requiring large atom-pump detuning Δ_a, we can adiabatically eliminate the excited atomic states. Using the Heisenberg equations of motion $\frac{\partial \Psi_e(\boldsymbol{x})}{\partial t} = \frac{i}{\hbar}[H, \Psi_e(\boldsymbol{x})] = 0$, we can solve for $\Psi_e(\boldsymbol{x})$ and insert it back into the equations of motion of the ground states and the cavity fields. From there we can find an effective Hamiltonian H_{eff} which describes the dynamics with the excited states eliminated. We find

$$\begin{aligned} H_{eff} = \int d^3\boldsymbol{x} \Psi_g^\dagger(\boldsymbol{x}) \Big\{ & -\frac{\hbar^2}{2m}\nabla^2 + V_g(\boldsymbol{x}) \\ & + \frac{\hbar}{\Delta_a}[h^2(\boldsymbol{x}) + g^2(\boldsymbol{x}) a^\dagger a + h(\boldsymbol{x}) g(\boldsymbol{x})(a + a^\dagger)] \Big\} \Psi_g(\boldsymbol{x}) \\ & + \frac{U}{2} \int d^3\boldsymbol{x} \Psi_g^\dagger(\boldsymbol{x}) \Psi_g^\dagger(\boldsymbol{x}) \Psi_g(\boldsymbol{x}) \Psi_g(\boldsymbol{x}) \\ & - i\hbar\eta(a - a^\dagger) - \hbar\Delta_c a^\dagger a. \end{aligned} \tag{2.14}$$

From this point it is easier to switch back to the single particle Hamiltonian, make the appropriate assumptions and simplifications for our model and then again go back to the many-body formalism. The single particle Hamiltonian (2.14) is easy to write down as

$$\begin{aligned} H_{eff}^{(1)} = & \frac{\boldsymbol{p}^2}{2m} + V_g(\boldsymbol{x}) + \frac{\hbar}{\Delta_a}[h^2(\boldsymbol{x}) + g^2(\boldsymbol{x}) a^\dagger a + h(\boldsymbol{x}) g(\boldsymbol{x})(a + a^\dagger)] \\ & - i\hbar\eta(a - a^\dagger) - \hbar\Delta_c a^\dagger a. \end{aligned} \tag{2.15}$$

In our model we illuminate the atoms directly by laser light. This means that light gets scattered by the atoms, independently into the corresponding cavity modes. Therefore we can set $\eta = 0$. We choose the cavity to be along the x-direction. An additional external dipole trapping potential [19] creates a lattice inside the cavity, confining the atoms, even when there are no photons in the cavity. Hence, we introduce $V_g = V_L \cos^2(k_L x)$. The mode function of the cavity can be approximated by a standing wave $g(\boldsymbol{x}) = g_0 \cos(k_c x)$, for a cavity in the x-direction. The perpendicular driving of the atoms along the y- direction can also be assumed to be a standing wave with $h(x) = h_0 \cos(k_p y)$. Assuming that the 1D lattice is centered at $y = 0$, $h(x)$ reduces to a simple constant, uniformly driving the whole lattice. Since we are interested in the dynamics, the resulting constant shift due to $h^2(x)$ can

be omitted.
The resulting one-particle Hamiltonian can then be written as

$$H_{eff}^{(1)} = \frac{p^2}{2m} + V_L \cos^2(k_L x) - \hbar(\Delta_c - U_0)a^\dagger a + \frac{\hbar}{\Delta_a} h_0 g_0 \cos(k_c x)(a + a^\dagger), \tag{2.16}$$

where we have defined $U_0 = g_0^2/\Delta_a$.

Using this simplified Hamiltonian we go back to the many-body formalism. For that we expand the ground state field operators into maximally localized single atom Wannier functions [30]

$$\Psi_g(x) = \sum_n \sum_k b_{n,k} w_n(x - x_k), \tag{2.17}$$

where $b_{n,k}$ corresponds to the annihilation of a particle in the n-th energy band at site k. Assuming only small energies we can restrict the Wannier functions to the lowest energy band $n = 0$ and therefore write $\Psi_g(x) = \sum_k b_k w(x - x_k)$. Using this expansion we also restore the particle-particle interaction as

$$U_{ijkl} = 4\pi a_s \hbar^2/m \int dx w(x - x_i) w(x - x_j) w(x - x_k) w(x - x_l), \tag{2.18}$$

We can omit the off-site terms of the nonlinear interaction matrix elements since they are typically two orders of magnitude smaller than the on-site elements [37] and (2.18) reduces to $U = 4\pi a_s \hbar^2/m \int dx \, |w(x)|^4$. The many-body Hamiltonian now takes the Bose-Hubbard type form

$$\begin{aligned} H = &\sum_{m,n} J_{m,n} b_m^\dagger b_n - \hbar\big(\Delta_c - U_0 \sum_n b_n^\dagger b_n\big) a^\dagger a \\ &+ \hbar \sum_{m,n} \tilde{J}_{m,n} b_m^\dagger b_n (a + a^\dagger) + \frac{U}{2} \sum_k b_k^\dagger b_k (b_k^\dagger b_k - 1), \end{aligned} \tag{2.19}$$

where we have defined the m to n site hopping element and pump-strength as

$$J_{m,n} = \int dx w(x - x_m) \big(- \frac{\hbar^2}{2m} \nabla^2 + V_L \cos^2(k_L x) \big) w(x - x_n) \tag{2.20}$$

$$\tilde{J}_{m,n} = \int dx w(x - x_m) \cos(k_c x) w(x - x_n). \tag{2.21}$$

Simplifying further, we use the tight-binding approximation [23] and hence ignore the next-nearest-neighbor terms. We also neglect the on site hopping terms, considering that they only amount to additive constants. By taking a closer look at $\tilde{J}_{m,n}$ one realizes that these change signs periodically due to the cos- function, i.e., $\tilde{J}_{n,n} = -\tilde{J}_{n+1,n+1}$, and furthermore this also accounts for $\tilde{J}_{k,k+1} = 0$.

Finally we neglect the U_0 atom-photon back action to reduce the complexity of our model. We now end up with the basic Hamiltonian that will describe all the dynamics we are interested in. Using the number operator $n_k = b_k^\dagger b_k$ one can finally define

$$H = J\sum_k (b_k^\dagger b_{k+1} + h.c.) + \frac{U}{2}\sum_k n_k(n_k - 1) - \hbar\Delta_c a^\dagger a + (a + a^\dagger)\sum_k \tilde{J}_k n_k. \tag{2.22}$$

2.1.2 Four sites - two Modes - model

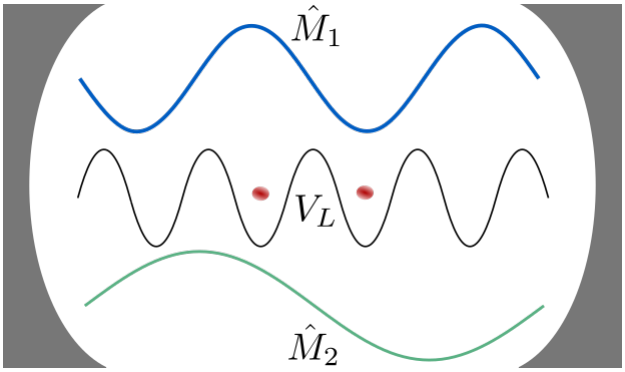

Figure 2.2: Visualization of the model with two particles, restricted to four lattice sites and two cavity modes, described by the mode operators $\hat{M}_1$ and $\hat{M}_2$ (see text below).

Having derived the general Hamiltonian (2.22) we need to further simplify the model, to the point where we can solve it at least numerically. First of all, we will restrict the lattice to four sites, i.e., the summation over the site index will reduce to $k \in \{1, 2, 3, 4\}$. Due to the periodic structure all sites are equivalent. It is sufficient for investigating the behavior and also is a necessary simplification for simulations. Also we impose periodic boundary conditions,

which means that particles in the most left potential well can jump to the most right one and vice versa. The associated particle Hamiltonians are

$$H_{tun} = J \sum_{k_{PBC}} (b_k^\dagger b_{k+1} + h.c.),$$
$$U_{int} = \frac{U}{2} \sum_k n_k(n_k - 1),$$

where $k \in \{1, 2, 3, 4\}$ and k_{PBC} denotes the periodic boundary conditions.

For introducing just enough complexity into our model we include a second field mode into our system. As we will see later this is already complex enough so that quantum effects play a vital role.
This can be done without going through the calculations above. Looking at the last term in (2.22) we can generalize this concept. Considering that the atoms are confined to the four lattice sites due to an additional potential V_L and that there is no scattering of photons between the two field modes, i.e., big enough frequency spacing between the modes, we can introduce m modes simply by modifying $\sum_m \sum_k \tilde{J}_{k,m} \hat{n}_k (a_m + a_m^\dagger)$, where a_k will annihilate a photon in the m-th mode and $\tilde{J}_{k,m}$ is the mode specific interaction strength. Note that adding a mode in our model, physically implies adding a pump laser with a mode specific detuning $\Delta_c^m = \omega_p^m - \omega_c^m$, inducing the scattering into the specific mode. For our purpose we will use two different modes, where one has twice the wave length of the other. Incorporating this we rewrite the interaction term as

$$H_{int} = \tilde{J}\big(\hat{M}_1(a_1 + a_1^\dagger) + \hat{M}_2(a_2 + a_2^\dagger)\big), \tag{2.23}$$

and introduce the effective mode scattering operators $\hat{M}_1 = (-\hat{n}_1 + \hat{n}_2 - \hat{n}_3 + \hat{n}_4)$ and $\hat{M}_2 = (+\hat{n}_1 + \hat{n}_2 - \hat{n}_3 - \hat{n}_4)$. The periodicity of the modes is now described by the mode-operators and the pump-strength $\tilde{J}$, where we have absorbed the sign of the mode-functions into $\hat{M}_1$ and $\hat{M}_2$. A visualization is shown in figure 2.2. In course of this theses we will often talk of potential wells instead of lattice sites, as it is a more visual description of the physics behind the model. The interaction strength $\tilde{J}$ is now a constant factor equal for all modes and lattice sites. Also the radiation Hamiltonian has to be modified to incorporate different modes and pump lasers. By dropping the c subscript in Δ_c^m and assuming equal detuning of the two modes we can write it as

$$H_{rad} = -\Delta(a_1^\dagger a_1 + a_2^\dagger a_2). \tag{2.24}$$

Keeping in mind that Δ here is the cavity-pump detuning, we can make sure that the detuning of both modes are equal by adjusting the pump frequencies ω_p^1 and ω_p^2. The full Hamiltonian finally reads

$$\begin{aligned} H =& J \sum_{k_{PBC}} (b_k^\dagger b_{k+1} + h.c.) + \frac{U}{2} \sum_k n_k(n_k - 1) \\ & - \Delta(a_1^\dagger a_1 + a_2^\dagger a_2) + \tilde{J}\big(\hat{M}_1(a_1 + a_1^\dagger) + \hat{M}_2(a_2 + a_2^\dagger)\big). \end{aligned} \tag{2.25}$$

2.1.3 Master equation

In general we should also take into account two forms of dissipation, the loss of photons through the cavity mirrors and the spontaneous emission of photons. The latter will scale by $\propto \frac{1}{\Delta_a^2}$ and will be suppressed by a large atom-pump detuning Δ_a, hence we will neglect it. We still have to incorporate the cavity loss κ. This is usually done in the master equation formalism, which tells us the evolution of the atom-field density matrix by

$$\dot{\rho} = -\frac{i}{\hbar}[H, \rho] + \mathcal{L}[\rho], \tag{2.26}$$

$$\mathcal{L}[\rho] = \sum_{m \in \{1,2\}} \kappa_m (2a_m \rho a_m^\dagger - a_m^\dagger a_m \rho - \rho a_m^\dagger a_m), \tag{2.27}$$

where the Liouvillean $\mathcal{L}$ is a standard quantum optics approach to modeling the dissipation [9]. The density operator is in our case given by the composite fock spaces of the lattice sites and the two photon modes $\rho = |\psi\rangle\langle\psi|$ with $|\psi\rangle = |n_1, n_2, n_3, n_4\rangle_A \bigotimes |n_1, n_2\rangle_{ph}$.

2.1.4 Adiabatic and semi-classical description

From (2.23) and (2.24) we can calculate the Heisenberg equations for the field operators $\dot{a}_m = \frac{i}{\hbar}[H_{rad} + H_{int}, a_m]$ to be

$$\dot{a}_m = i\Delta a_m - i\tilde{J}\hat{M}_m - \kappa_m a_m. \tag{2.28}$$

The dissipation of photons through the cavity mirror with rate κ_m is accounted for. To construct an effective particle Hamiltonian, it is possible to adiabatically eliminate the cavity fields (2.28). This is valid if the field dynamics, governed by κ_m and Δ, are of a faster time scale than the atomic

tunneling processes, i.e., $J/\hbar \ll |\Delta + i\kappa|$. This means that relative to the time scale of the atomic motion, the fields will always be in a steady state. Therefore we formally set $\dot{a}_m = 0$ and solve for a_m, leaving us with

$$a_m = \frac{-i\tilde{J}}{\kappa_m - i\Delta}\hat{M}_m. \tag{2.29}$$

Feeding this back into (2.23) and (2.24), the atom-light interaction is described by an effective interaction of the particles, in the coherent regime $|\Delta \gg \kappa|$. The effective Hamiltonian then reads

$$H = H_{tun} + U_{int} + H_{ad}, \tag{2.30}$$

$$H_{ad} = \frac{\Delta\tilde{J}^2}{\kappa^2 + \Delta^2}\big(\hat{M}_1^2 + \hat{M}_2^2\big). \tag{2.31}$$

Instead of considering the full quantum fields, we can further approximate the dynamics and assume classical fields $\alpha_m(t)$ for the two modes, which amounts to a factorized atom-field state. This is done by replacing the field operators by their expectation values $\langle a_m \rangle = \alpha_m(t) \in \mathbb{C}$ in (2.23) and (2.24), where

$$\alpha_m(t) = \frac{-i\tilde{J}}{\kappa_m - i\Delta}\langle \hat{M}_m \rangle. \tag{2.32}$$

The $\langle \hat{M}_m \rangle$ here denotes the expectation value of the mode operators. We finally get a new approximative semi classical Hamiltonian, where the fields are represented simply by complex numbers

$$H_{ad}^{sc} = \frac{\Delta\tilde{J}^2}{\kappa^2 + \Delta^2}\big(2\hat{M}_1\langle \hat{M}_1 \rangle - \hat{\mathbb{I}}\langle \hat{M}_1 \rangle^2 + 2\hat{M}_2\langle \hat{M}_2 \rangle - \hat{\mathbb{I}}\langle \hat{M}_2 \rangle^2\big). \tag{2.33}$$

The $\hat{\mathbb{I}}$ denotes the identity operator and has dimension of the particle Hilbert space. We will be considering two particles within our four lattice sites, i.e. half filling. Accordingly, for four wells, defined as Fock-states with occupation numbers $\{0, 1, 2\}$, to allow for at most two particle occupations, the dimension of the space is $3^4 = 81$. Comparing (2.33) and (2.30) the big difference is in the quadrature of the mode operators. In the semi-classical case the fluctuations are of first order around the mean of $\hat{M}_1$ and $\hat{M}_2$. This has the effect that while for the adiabatic Hamiltonian, effective particle-particle

entanglement introduced by the light fields are included, in the semi-classical model there can be no entanglement. As classical fields can not be in superposition states. To solve the Schrödinger equation for the semi-classical model, one has to evaluate the expectation values of the mode operators self-consistently for each timestep.

2.2 Quantum annealing

In this chapter we will introduce the main concepts of quantum annealing [28]. Its primary perspective is to find the global minimum of a given cost function by using quantum degrees of freedom. The promise of using quantum annealing is to achieve a significant speed up over classical heuristic optimization tools. Whether or not this is actually the case is still open to debate [21]. Nonetheless has there been serious technological progress in the industry as in research (e.g. D-Wave [25]). In the following we will first introduce the optimization problems that quantum annealing tries to address. Further we will give a mathematical interpretation with the adiabatic approximation. And finally we will apply the scheme to our model introduced in section 2.1.1.

2.2.1 Optimization problems

The prime application of quantum annealing is to solve classical combinatorial optimization problems. They involve finding optimal solutions to objective functions from a finite and discrete set of feasible solutions. Although, those problem can also be approached without quantum technology, many of those problems are NP-hard or NP-complete and hard to tackle by classical algorithms. Typical examples for classical combinatorial optimization problem are the traveling salesman [26] or the knapsack problem. Granting, solving the former examples with quantum speed up would be an valuable advancement, there are more physical and scientific issues where quantum annealing could be a useful tool. A few examples are quantum chemistry [5], machine learning [34] or protein folding [38]. This is where quantum annealing comes in and offers the promise of faster and more optimal solutions. Although, a general speed up over classical algorithms is not clear, there are examples where quantum annealing seems promising (e.g., [1]). In contrast to simulated annealing, or other cost function minimization procedures like

variations of Monte Carlo simulation, the idea behind quantum annealing is to use quantum tunneling processes to make the search for a global minimum more efficient [28].

To use the idea of quantum annealing for general optimization problems of a given species, we need a generic procedure of translating the classical system into a quantum system. A well known and used example is the mapping onto a Ising spin glass system [16]. Many of those problems can be expressed in terms of binary variables $\{0, 1\}$ and two local interactions [35]. They are called quadratic unconstrained binary optimization problems (QUBO) [21] with a cost function of the form

$$H = \sum_{ij} J_{ij} s_i s_j + \sum_i c_i s_i. \tag{2.34}$$

The optimization problem is fully described by the coefficients J_{ij} and c_i. For higher order interactions, the system can be reduced to a quadratic structure with the help of auxiliary variables. QUBOs are very convenient as they can be mapped onto the classical Ising Model

$$H_{SG} = -\sum_{ij} J_{ij} \sigma_i^z \sigma_j^z + \sum_i h_i \sigma_i^z, \tag{2.35}$$

with the classical variable $\sigma_i^z = \pm 1$. Promoting these to quantum spin operators, the solution to the optimization problem will be encoded in the ground state of the system. Now, choosing an initial state which is easily prepared and adiabatically switching on H_{SG}, the state will remain in the ground state and assume approximately the solution, according to the adiabatic approximation (2.2.2). An obvious choice for the initial Hamiltonian for example would be $H_0 = -h_0 \sum_i \sigma_i^x$, as its ground state prepares the system in an superposition of all possible states in the computational basis of H_{SG}.

In analogy to this we are considering a very similar set up. Looking at the Hamiltonian (2.25) the initial state will be due to the tunneling part H_{tun}, which will prepare a superposition of all lattice sites, much in the same way as H_0 does for the Ising model. The optimization problem will then be given by the interaction term H_{int}, where the energy landscape is given by the competing mode functions. The implementation of the quantum annealing procedure into the given model will be done more carefully in section 2.2.3. In the next section we will introduce the basis for the adiabatic optimization.

2.2.2 Adiabatic approximation

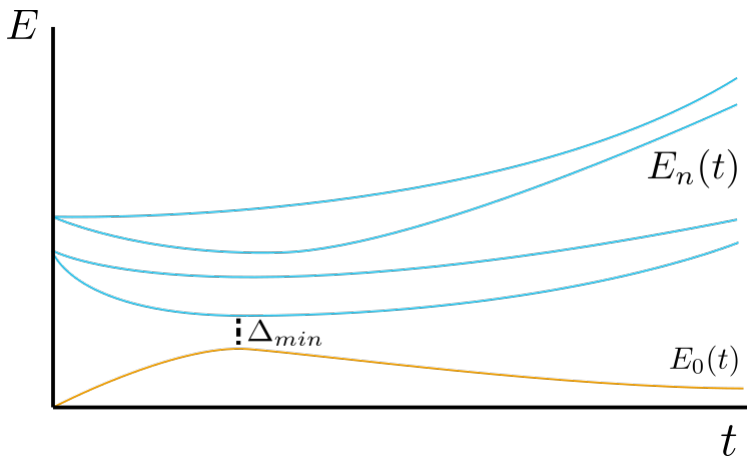

Figure 2.3: Illustrative example of the energy spectrum as a function of time. Shown is the ground state energy $E_0(t)$ in orange with the characteristic minimal energy gap Δ_{min}. The blue lines correspond to the higher energy levels $E_n(t)$.

An important starting point in the discussion of the quantum annealing is the adiabatic approximation [8]. It states as follows: A quantum system prepared in an eigenstate $|\Psi_n(0)\rangle$ of a time-dependent Hamiltonian $H(t)$, evolving according to the Schrödinger equation

$$i\frac{\partial|\Psi(t)\rangle}{\partial t} = H(t)|\Psi(t)\rangle, \tag{2.36}$$

will stay approximately in the instantaneous eigenstate $|\Psi_n(t)\rangle$ of $H(t)$, given that the Hamiltonian changes "sufficiently slow". In practice one will often use the ground state $|\Psi_0(t)\rangle$.

This basic idea has been proven in more rigorous forms as the adiabatic theorem. In the following we will introduce one of the most common and simplest forms of the approximation [17]. Even though it has been criticized [36] as not being sufficient and rigorous proofs of the theorem are available (e.g.,[29]), the qualitative statement of the approximation stays the same and will be sufficient for our discussion.

Let $|\Psi_n(t)\rangle$ be the instantaneous eigenstate of an Hamiltonian $H(t)$, with energy $E_n(t)$ and $n \in \{0, 1, 2, ...\}$ denoting the energy levels. The spectrum

is such that $E_n(t) \leqslant E_{n+1}(t)\ \forall n, t$, $n = 0$ being the ground state and obeying $H(t)|\Psi_n(t)\rangle = E_n(t)\,|\Psi_n(t)\rangle$. Assuming that the initial state is prepared in any eigenstate $|\Psi_n(0)\rangle$, the system will stay close to the instantaneous eigenstate $|\Psi_n(t)\rangle$ for all $t \in [0, t_f]$, with t_f being the final time, under the condition that

$$\max_{t\in[0,t_f]} \frac{|\langle\Psi_n|\,\partial_t H\,|\Psi_m\rangle|}{|E_n - E_m|^2} \ll 1 \quad \forall n \neq m. \tag{2.37}$$

Counterexamples, where the adiabatic condition (2.37) does not hold are well known [36]. One example is the case when the Hamiltonian is subject to a time-dependent parameter whose time-scale is faster than the time-scale of the the internal energy-scale. This can lead to oscillations in the eigenstate population even if (2.37) is fulfilled.

This problematic behavior can be circumvented by considering Hamiltonians whose time-dependence is parameterized by a single variable $s = t/t_f$ where $s \in [0, 1]$. The situation where the Hamiltonian can be written dependent on this parameter $H(t) = H'(s)$ is used in most theoretical works on quantum annealing. It is useful then to write it as an interpolation of two different Hamiltonians which do not commute,

$$H'(s) = A(s)\ H_0 + B(s)\ H_1, \tag{2.38}$$

a starting Hamiltonian H_0 and a problem one H_1, where the solution to the optimization problem is encoded in the ground state of H_1. The factor $A(s)$ and $B(s)$ can be chosen to be monotonically decreasing and increasing, respectively.

In most cases one is only interested in the ground state. Introducing $\Delta_{1,0}(s) = E_1(s) - E_0(s)$ as the energy gap between ground state and the first excited state and dropping the prime in $H'(s)$, the adiabatic approximation can be redefined in terms of s and takes the form

$$\max_{s\in[0,1]} \frac{|\langle\Psi_1(s)|\,\partial_s H(s)\,|\Psi_0(s)\rangle|}{\Delta_{1,0}(s)^2} \ll t_f. \tag{2.39}$$

Defining the minimum of the energy gap as $\Delta_{min} = \min_s \Delta_{1,0}(s)$, the adiabatic transition time t_f is often analyzed in terms of the minimal squared inverse energy gap $1/\Delta_{min}^2$. An illustrative energy spectrum fulfilling this condition is shown in figure 2.3. As mentioned, more rigorous conditions can be derived in form of adiabatic theorems (e.g., by Kato [29]), but are not of utter importance for our discussion, since the efficiency analysis is not the main goal of this thesis.

2.2.3 Applying quantum annealing to the model

Let us now apply the discussion from the previous section to our physical model derived in chapter 2.1.1. We need to apply the interpolation scheme $H(s) = A(s)\ H_0 + B(s)\ H_1$ to our model Hamiltonian (2.25). For that we need to identify the initial Hamiltonian H_0 and the problem Hamiltonian H_1. As initial condition we want our particles to sit in an optical lattice inside the cavity without coupling to the pump laser. Therefore they will be subject to tunneling H_{tun} and on-site interaction U_{int}. We also add the radiation Hamiltonian (2.24) since this will have no effect in the beginning, as there are no photons present. Therefore we define $H_0 = H_{tun} + H_{rad} + U_{int}$. The problem Hamiltonian is therefore the remaining interaction part $H_1 = H_{int}$. This means that the optimization physically amounts to the ordering of the particle due to the mode-functions, formally determined by $\hat{M}_1$ and $\hat{M}_2$.

Finally the time-dependent coefficients $A(s)$ and $B(s)$ need to be determined in a suitable way. One popular choice is to set $A(s) = 1$ and $B(s) = s = t/t_f$. This comes very natural to our choice of initial and final Hamiltonian. Tunneling and particle-particle interactions are therefore independent of time and will not change, which seems reasonable for a experimental setup, where the controlled variation of these parts would be rather complicated. We also want the detuning Δ to be constant during the adiabatic scheme and applying the time-dependence to H_{rad} would physically translate to a change in the pump laser frequency. In contrast to that, a time-dependence in the interaction Hamiltonian would represent a controlled increase in the laser-field intensity which is feasible in laboratory conditions. To indicate this we absorb $s = \frac{t}{t_f}$ into the interaction parameter as $\tilde{J}(s) = \frac{t}{t_f}\ \tilde{J}\ \in [0, \tilde{J}]$. We now have the model setup for our quantum annealing protocol

$$\begin{aligned} H(s) =& J \sum_{k_{PBC}} (b_k^\dagger b_{k+1} + h.c.) - \Delta(a_1^\dagger a_1 + a_2^\dagger a_2) + \frac{U}{2} \sum_k n_k(n_k - 1) \\ &+ \tilde{J}(s) \left(\hat{M}_1(a_1 + a_1^\dagger) + \hat{M}_2(a_2 + a_2^\dagger) \right). \end{aligned} \tag{2.40}$$

With the current choice of parameters and our mode functions, the ground state of $H_{int} = \tilde{J}\ \left(\hat{M}_1(a_1 + a_1^\dagger) + \hat{M}_2(a_2 + a_2^\dagger) \right)$ is degenerate. The two solutions for the ground state correspond to two possibilities per mode. For $\hat{M}_1$ the two degenerate ground states are fixed by $\langle \hat{n}_1 \rangle = \langle \hat{n}_3 \rangle = 1$ and $\langle \hat{n}_2 \rangle = \langle \hat{n}_4 \rangle = 1$, i.e. each particle at one site, determined by the signs

in the mode operator. Equivalently the ground states of $\hat{M}_2$ are fixed by $\langle\hat{n}_1\rangle = \langle\hat{n}_2\rangle = 1$ and $\langle\hat{n}_3\rangle = \langle\hat{n}_4\rangle = 1$. To incorporate a single solution we have to modify the mode-functions in a way that the energy levels are split into a single ground state and arbitrary excited states with an energy gap. This can be done by artificially changing the depth of one potential well. Integrating an additional depth factor V the mode operators are adjusted as

$$\hat{M}_1 = (-\hat{n}_1 + \hat{n}_2 - V\hat{n}_3 + \hat{n}_4), \tag{2.41}$$

$$\hat{M}_2 = (+\hat{n}_1 + \hat{n}_2 - V\hat{n}_3 - \hat{n}_4). \tag{2.42}$$

With $V > 1$ we lift the degeneracy in the ground state of the energyspectrum and design a single solution corresponding to a two particle state for the third lattice site. The system evolves according to the Schrödinger equation (2.36) from an initial state, chosen as the ground state of $H(0) = H_{tun} + U_{int} + H_{rad}$, by an adiabatic evolution into the ground state of the full Hamiltonian. The evolution time will then be fully determined by the value of t_f, this means that for higher values the system will take longer to evolve and therefore undergo a slower evolution.

The initial state will be the ground state of the BM-Hamiltonian $H(0) = H_{tun} + U_{int} + H_{rad}$ and can be easily numerically computed. Analytically the initial state is a tensor product of the particle and photon ground state $|\Psi_0(0)\rangle_{particle} \otimes |\Psi_0(0)\rangle_{photons}$. For the photon part it is clear that the initial state subject to H_{rad} is the 0-photon Fock state for both modes $|\Psi_0(0)\rangle_{photons} = |0;0\rangle_{ph}$. For the particles it is not as obvious. The ground state of H_{tun} is the superfluid state

$$|SF\rangle = \frac{1}{\sqrt{N}}\Big(\sum_{k=1}^{n}\frac{b_k^\dagger}{\sqrt{n}}\Big)^N|vac\rangle\,, \tag{2.43}$$

with N being the number of particles, n the number of sites and $|vac\rangle$ being the vacuum state with no particles. However, the real ground state of the system will be different due to the on-site interaction U_{int}. The particle repulsion will disturb the superfluid state, where the particles are in a superposition of the well occupation, towards a Mott-insulator state, where a definite position of the particles is known. This phase transition is well known in the studies of the Bose-Hubbard model [33]. Although, an analytical computation of the full ground state is fairly complicated, the distortion of the superfluid state due to U will be discussed in section 3.1.2 and turns out to be rather small.

2.3 Self-organization in optical systems

An important phenomenon appearing for ultracold atoms inside optical cavities is self-organization. As self organization one understands the structured arrangement of the particles from an unorganized setup, as a result of intrinsic interactions. In the context of ultracold atoms this leads to the formation of a periodic lattice from a chaotic quantum gas [40]. Considering the direct pumping of atoms, light gets scattered coherently from the atoms into the cavity fields. These fields interfere with the pump laser and induce collective interactions between the atoms. This interaction creates a force, influencing the motion of the atoms, which again influence the fields. An effective atom-atom interaction is created mediated by the cavity photons. This dynamical behavior of the whole system then leads to a crystallized organization of the particles above a laser threshold [4], where the stabilizing effects of thermal fluctuations are overcome.

Let us assume that we have a high-Q optical cavity and the scattered light generates a standing wave inside the cavity. We can approximate the mode-function by a sinusoidal $sin(kx)$ with a wavelength λ and a wave number $k = 2\pi/\lambda$. By transversal pumping of the atoms, the laser field creates an optical potential, which will create a dipole force on the atoms. In case of red detuning $\Delta 0$ of the laser, the atoms will move into the region of high intensity, i.e., the antinodes of the standing wave [14]. As the periodicity of the sinus antinodes is $\lambda/2$, the scattered light from atoms distanced by $\lambda/2$ will destructively interfere. But as it turns out, the particles will occupy spaces separated by λ to maximize the scattered light thorough constructive interference, also called super-radiance [13]. This will lead to the characteristic even-/ odd- site occupation of the crystallized atoms.

Chapter 3

Simulations and Results

3.1 Analysis of the full quantum dynamics

In the following sections we will give an in depth analysis of the most important features of the chosen model, with respect to the quantum annealing procedure. Hence, we will start with a discussion of the energy spectrum, the minimum gap and its dependence on the additional well depth V. Afterwards there will be a general discussion about the chosen parameters and their effect on the system, especially on the numerical cut-off. Finally we will look at the solution quality dependent on the simulation time and the connection to the field-particle entanglement.
For all simulations the given parameters are either chosen in units of the recoil energy $\hbar\omega_r = \hbar\,\frac{\hbar k^2}{2m}$ corresponding to the change of energy an atom with mass m sustains, by absorbing or emitting a photon with wavevector k, or in units of the recoil frequency ω_r itself. In the following sections we will mostly omit this whenever we describe the parameter values, considering that for the dynamics of our system only the relative values are of importance.

3.1.1 Energy spectrum

In this section we first investigate the energy spectrum of the full quantum Hamiltonian (2.40). For this we numerically solve the eigenvalue problem $H(s)\,|\psi_n(s)\rangle = E_n(s)\,|\psi_n(s)\rangle$ for a number of eigenvalues n with $s \in [0, 1]$, and we plot them as a function of $\tilde{J}(s)$. Note that all of the numerical work in this theses, is done by using the QuantumOptics.jl package [31] for the Julia programming language. In figure 3.1 the lowest 10 eigenenergies are depicted.

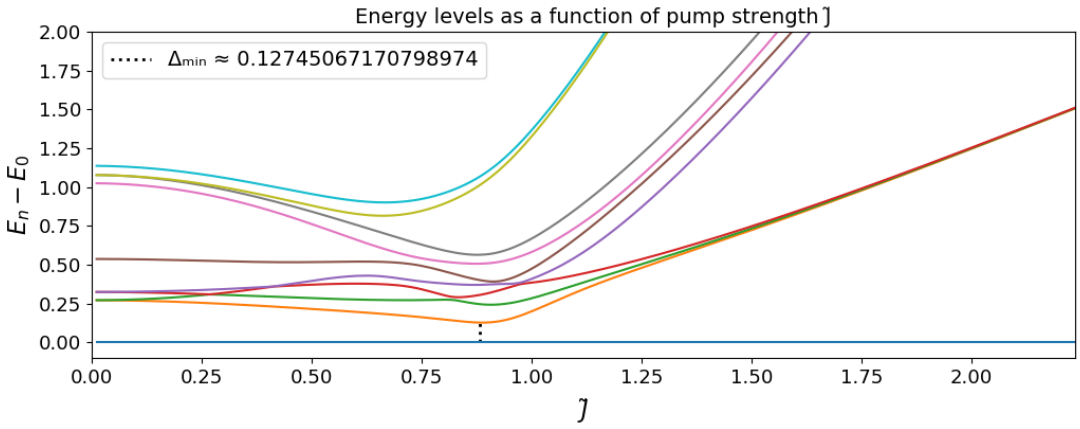

Figure 3.1: Energy-spectrum of the full quantum Hamiltonian (2.40) up to the 10th eigenstate. Energies are plotted relative to the ground state as a function of $\tilde{J}(s)$ with $s \in [0, 1]$. Minimum energy gap between ground and first excited state is depicted with $\Delta_{min} \approx 0.1275$. System parameters are chosen to be: $J = 0.1$, $U = 0.7$, $V = 1.1$, $\tilde{J}^2 = 5 = \Delta$.

They are plotted relative to the ground state energy as $E_n(s) - E_0(s)$, where n denotes the excitation level. At this point one should mention that we need to introduce a numerical approximation for the photon Fock state, to allow for simulation. As the Hilbert space of a field mode (= harmonic oscillator) has infinite dimension we would exactly represent it in a coherent state. We need to work with finite matrices and therefore it is necessary to introduce a photon state cut-off. This reduces the dimension of the Hilbert space and makes numerical simulations feasible. We already mentioned in section (2.1.4) that the dimension of the particle space is $3^4 = 81$. For two modes, the Hilbert space increases by a factor of $(nc + 1)^2$, where nc is the photon cut-off. Hence, we choose for most of our simulations a photon cut-off $nc = 3$ which reduces the full dimension of our system to $3^4 * 4^2 = 1296$. The down side is, of course, that this artificial limitation is not physical and hence we loose the dynamics involving higher occupational states. The justification of the chosen cut-off and further investigations will be done in section 3.1.2.

Coming back to the figure, the minimum energy gap between the ground and first excited state is marked, as it is an important quantity. As it is mandatory for quantum annealing, the model shows a distinct, non-degenerate ground state with a energy gap to the first excited state. We can also explain

the behavior of the lowest three excited states. If we set the extra shift of one site $V = 0$ in (2.41), there are four degenerate solution to H_{int}, two for each mode. As we lower one potential well by $V > 1$, we lift this degeneracy and pick out one unique ground state. The fact that the lowest three excited states converge is due to the fact that they are still degenerate, as we have 3 equal sites.

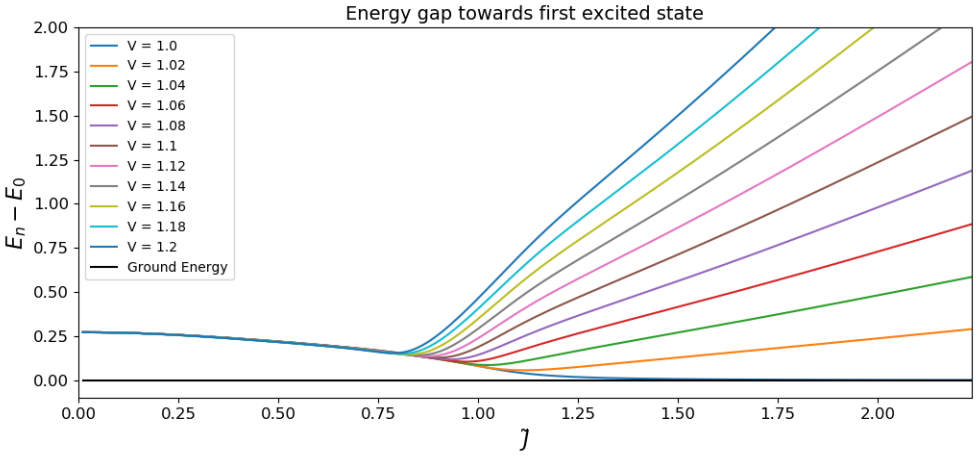

Figure 3.2: First excited state energy for different well depth V. Energies are plotted relative to the ground state as a function of $\tilde{J}(s)$ with $s \in [0, 1]$. Opening of the energy gap and lifting of the degeneracy can be seen as V increases. System parameters are chosen to be: $J = 0.1$, $U = 0.7$, $V \in [1.0, 1.2]$, $\tilde{J}^2 = 5 = \Delta$.

In particular we will look at the dependence of the first excited state energy on V. This is done in figure 3.3. As one can easily see, for $V = 0$ the $n = 1$ state converges to the ground state. As the additional depth of the third well gets increased an energy gap opens. The behavior of the minimum gap can also be examined. According to the plot it opens for ever smaller values of $\tilde{J}$ as V increases. As the energies for different V do not change until the minimum gap opens, we can deduce that the scale of the gap as a function of V follows the excited energy curve from right to left. This is plotted in figure 3.3.

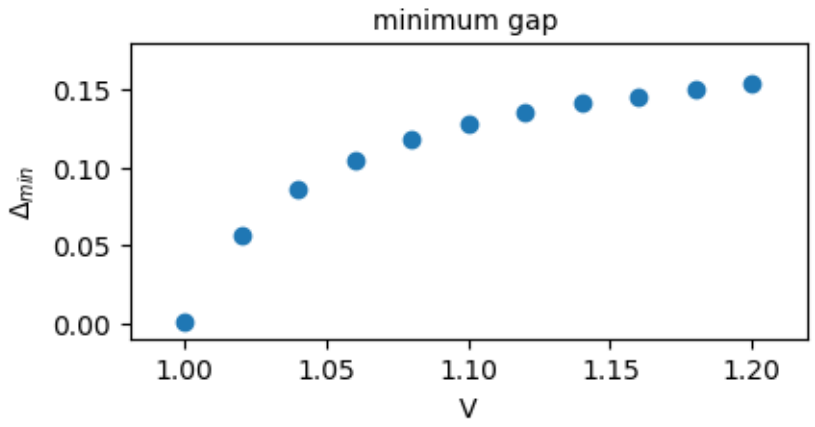

Figure 3.3: Evolution of the minimum energy gap between ground and first excited state as a function of the well depth V. System parameters: $J = 0.1$, $U = 0.7$, $V \in [1.0, 1.2]$, $\tilde{J}^2 = 5 = \Delta$

3.1.2 System parameters

Let us now take a closer look on the dynamics for different parameter values. Let us first talk about the site-to-site hopping amplitude J. It accounts for the particles probability to jump to neighboring lattice sites and corresponds to the kinetic energy term in the Hamiltonian. In the course of the thesis we will hold this parameter constant. This is reasonable for the following arguments. First off, the specific value of the parameter is not of grave importance. Only the relative magnitude in respect to the other system-parameters is of significance. Therefore keeping J at a specific value, while changing other constants, makes the investigation simpler without the loss of generality. Further, the jumping of the atoms is important in the beginning, as it allows the reordering of the system, but gets less influential as the system evolves into the ground state of the full Hamiltonian. Accordingly, choosing J as to fulfill the adiabatic condition (section 2.1.4) and being small compared to $\tilde{J}(s)$ for $s = 1$ (i.e., at the end of the sweep), is a reasonable decision for all simulations that we will present. Hence, we set $J = 0.1\ \hbar\omega_r$ which turns out to work well in our case.

The on-site particle-particle interaction is adjusted by the U parameter. There are a few things to consider. We already mentioned in section 2.2.3 that U influences the particle ground state of our initial system. For no

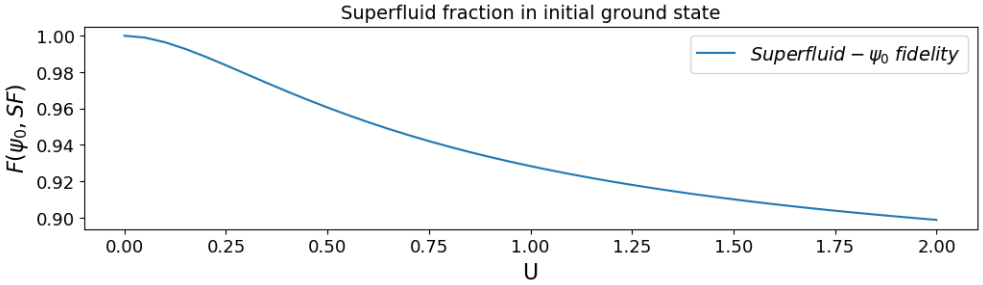

Figure 3.4: The fidelity of the initial Hamiltonian $H(0)$ grounds state and the ideal superfluid state as a function of the on-site interaction U.

on-site interaction we expect the particles to be in a maximally delocalized superfluid state, according to the ground state of H_{tun}. To see how strong the perturbation of the superfluid state is, we can use the fidelity defined as

$$F(\rho, \sigma) = Tr\left(\sqrt{\sqrt{\rho}\sigma\sqrt{\rho}}\right), \tag{3.1}$$

with $\sqrt{\rho} = \sum_n \sqrt{\lambda_n}\,|\psi\rangle\langle\psi|$. Here ρ and σ are two density operators, Tr denotes the trace and the square root of the positive semi-definite operator is given by the square root of the n eigenvalues given by the spectral theorem. We can now check the fidelity of the ideal superfluid state with the actual ground state of the initial Hamiltonian for a range of U parameter. Note that at $T = 0$ the density matrices describe pure states. In figure 3.4 the fidelity as a function of $U \in [0, 2]$ is depicted. One can see that the deviation from the superfluid state is not particularly huge, with a fidelity of about $\mathcal{F} \approx 0.9$ for the highest on-site interaction strength considered. Especially, for small U the initial state can be regarded as being in the superfluid state.

We already discussed the importance of the photon cut-off parameter nc in the previous section. Let us further justify the chosen cut-off by looking at the photon evolution and Fock state inside the cavity. If we want the finite cut-off to be as physical reliable as possible, it is important that there is only a negligible occupation of the highest Fock state considered. In our case of $nc = 3$ we assumes that the probability of occupying the three photon state $|3\rangle$ for both modes is small. Accordingly, also the cavity photon number should be small. To achieve this one can consider the energy cost of adding a single photon. This gets described by the radiation Hamiltonian $H_{rad} = -\Delta(\hat{a}_1^\dagger \hat{a}_1 + \hat{a}_2^\dagger \hat{a}_2)$. Considering a negative detuning $\Delta < 0$ the cost of adding

a photon in each mode is exactly Δ. A negative Δ corresponds to atom cooling in the cavity optomechanics context [14] and high intensity seeking atoms in self organization [37]. Therefore, increasing the value of Δ makes the occupation of higher photon states less probable. But, to keep the intensity high, with less photons available, we also have to increase the pump strength $\tilde{J}$. The intensity growth proportional to $\propto \tilde{J}^2$ [40], hence we increase the pump by $\tilde{J} = \sqrt{\Delta}$ such that the two parameters are of the same order.

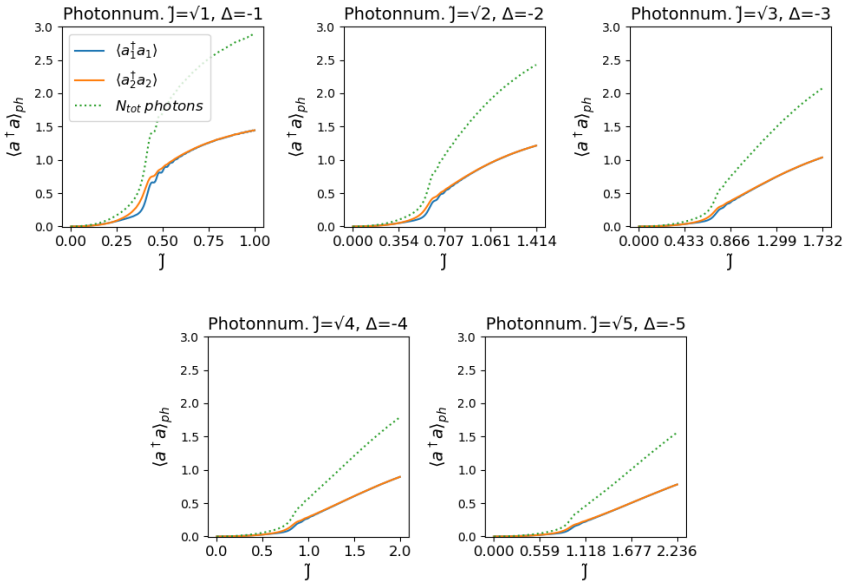

Figure 3.5: Evolution of the cavity photon numbers for both modes. The plots correspond to increasing parameters $\tilde{J}^2 = -\Delta \in \{1, 2, 3, 4, 5\}$ from left to right.

In figure 3.5 the evolution of the photon numbers are depicted, as a function of $\tilde{J}(s)$. Each plot corresponds to a different set of parameters, i.e., $\tilde{J}^2 = -\Delta \in \{1, 2, 3, 4, 5\}$. One can clearly see that by increasing the detuning and pumping strength the expectation value of the photon number shrinks by approximately the half. Hence, we can suppress the occupation of high photon numbers by increasing the detuning and therefore reduce the approximation of the photon cut-off. Also one can see that the distinct dynamics differ for the varying parameters. As the detuning and pump increase, the photon number evolution changes from a s-like curve to a linear increase

with an onset above a threshold. Furthermore, the threshold point, where the sudden increase in photon growth sets in, moves to higher values of the pumping strength.

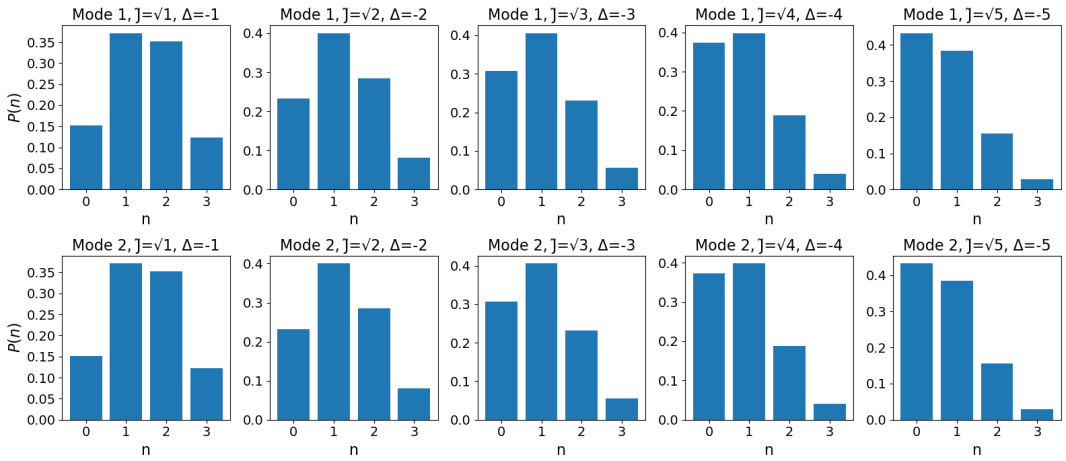

Figure 3.6: Photon state occupation probabilities at the end of the adiabatic evolution for changing pump strength and detuning $\tilde{J}^2 = -\Delta \in \{1, 2, 3, 4, 5\}$, from left to right. The upper and lower row correspond to the first and second mode given by $\hat{M}_1$ and $\hat{M}_2$, respectively.

From plot 3.6 a further assessment about the physicality of the chosen photon cut-off can be made. Here, the occupation probabilities for both modes at the end of the adiabatic evolution is plotted for different detunings and pumping strengths. By inspecting the first row one can clearly see that there is a significant amount of occupation in the third state. This tells us that the given state still plays an important role in the dynamics of the system. It further suggests that also higher states are relevant with non negligible population probabilities and therefore, the $nc = 3$ cut-off is a substantial alteration of the dynamics. Examining the rows from left to right, it is evident that the increase in Δ improves the approximation. For the most right plot, the majority of population is in the vacuum state $|0\rangle$ and only a minor occupation of the highest state is present. This further suggests the insignificance of higher order states. We therefore assume that the chosen cut-off is a good approximation and does not change the dynamic too much for a big enough detuning. Note that we cannot use low enough Δ, as some photons are needed to create interactions.

3.1.3 Simulation time and entanglement

In this section we will take a closer look at the finding evolution time the system needs, to achieve a high fidelity with respect to the correct solution. The higher the fidelity the lower the number of runs to obtain the solution. We already addressed the idea, that the system has to evolve sufficiently slow to allow for an adiabatic following of the system to stay in the ground state (see 2.2.2). Accordingly, we want to see how fast our optimization problem can be solved with small errors. We perform the adiabatic sweep for different simulation times, which is given by the choice of t_f. Considering a range of $t_f \in [10, 2000]$ we solve the Schrödinger equation for the Hamiltonian (2.40) and compute the fidelity between the final state of the evolution and the solution state. The correct final state is given by the lowest eigenstate of the full Hamiltonian. Choosing $\tilde{J}$ big enough such that at $t = t_f$ the eigenstate is dominated by H_1, and H_0 introduces only a small perturbation, we can assume that the lowest eigenstate of (2.40) is the correct solution to the optimization problem.

For the definition of the fidelity, the target state $|\Psi_{sol}\rangle$ can either be calculated directly by solving $H(1)\,|\Psi_0\rangle = E_0\,|\Psi_0\rangle \equiv E_0\,|\Psi_{sol}\rangle$ numerically, or by defining the solution directly by the state containing two particles on the third lattice site $\frac{1}{\sqrt{2}}(\hat{b}_3^\dagger)^2\,|vac\rangle$. Looking at the fidelity between the solution eigenstate and the defined state in the particle subsystem, one can see that they agree very well, i.e. the ground state of the full Hamiltonian is actually the state with two particles on the third lattice site $\hat{n}_3$.

In figure 3.7 the fidelity as a function of the simulation time t_f is plotted. For comparison we computed the same curve for the adiabatic Hamiltonian (2.30). On this scale the two curves agree very well, although the adiabatic Hamiltonian effectively incorporates photon loss through the cavity mirrors by introducing κ into the field Heisenberg equations. Therefore, it seems that at the chosen rate of $\kappa = 1\omega_r$ the effect of photon loss does not change the dynamics significantly. Already for a $t_f = 200$ a fidelity of $\mathcal{F} \approx 0.912$ is achieved, which is enough for solving the optimization problem. That the fidelity for very short times does not approach zero, is due to the fact that the initial state of the system $|\Psi_0\rangle$ has a nonzero overlap with the solution and which grows immensely with each time-step.

For very long transition times the fidelity looks like it converges to a maximum and a small distinction between the different Hamiltonians gets visible. To better see these discrepancy we plot the negative logarithm of

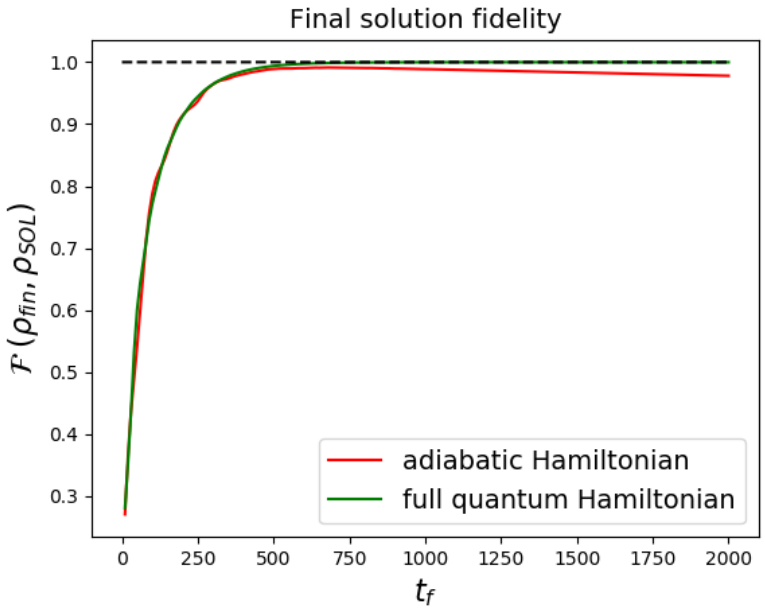

Figure 3.7: The fidelity between the final state after adiabatic evolution and the desired target state, as a function of simulation time. The green curve corresponds to the Hamiltonian with quantum fields (2.40) and the red one to the adiabatic model (2.30).

the infidelity, which is defined as the deviation of the fidelity from one, i.e., $(1 - \mathcal{F})$. Note that the minus sign is only for visual purposes. This is shown in figure 3.8. Here the differences can be seen more clearly. Already at about $t_f = 300$ the fidelity for the adiabatic Hamiltonian flattens and stops to improve. The accuracy of the full quantum Hamiltonian in contrast, improves further and reaches its maximum around a simulation time of $t_f \approx 1300$. From then on, longer simulations reduce the fidelity, therefore there seems to be an ideal simulation time which maximizes the fidelity.

In figure 3.9 the evolution of the state during the adiabatic sweep is plotted. On the left side the expectation value of site occupation $\langle \hat{n}_i \rangle$ is plotted. Starting from a distribution according to the superfluid state the occupation of the third site soon moves towards two particles. In the plot on the right side the fidelity with respect to different states is plotted. Note that although the fidelity for the final particle and mode subsystems increase separately, at the end of the sweep they always seem to be very close. Also

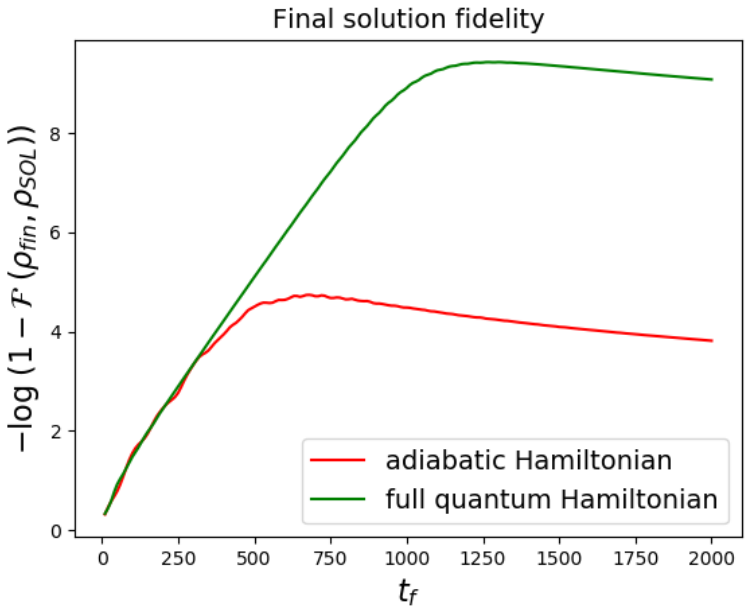

Figure 3.8: The negative logarithm of the infidelity between the final state after adiabatic evolution and the desired target state, as a function of simulation time. The green curve corresponds to the Hamiltonian with quantum fields (2.40) and the red one to the adiabatic model (2.30).

the evolution of the previously defined state with two particles in the third well is displayed and it can be seen that it is very close to the final particle state for $t \to t_f$.

As shown in Ref. [20], there is a connection between the entanglement remaining at the end of the adiabatic sweep and the success probability. To investigate the dynamics of entanglement in our system we will use the entanglement entropy. Considering two subsystems, A and B, the entanglement entropy is given by the Von Neumann entropy of the reduced density matrix $\rho_A = tr_B\rho$, where the reduced density is achieved by a partial trace over a subsystem. The Von Neumann entropy of the reduced state is then defined as

$$S_A = -tr(\rho_A log(\rho_A)). \tag{3.2}$$

In this and later sections we will look at two specific features of the entanglement. The maximum of the entanglement during one sweep and

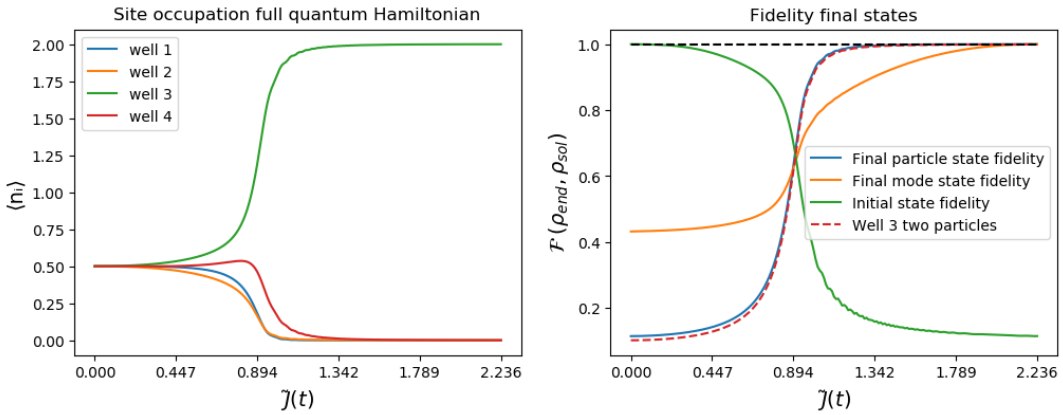

Figure 3.9: The state evolution of the full quantum Hamiltonian during one adiabatic seep is displayed. On the left side the expectation values of the lattice site occupations are plotted. The right plot shows the evolution of the fidelity between the system, solution and initial state.

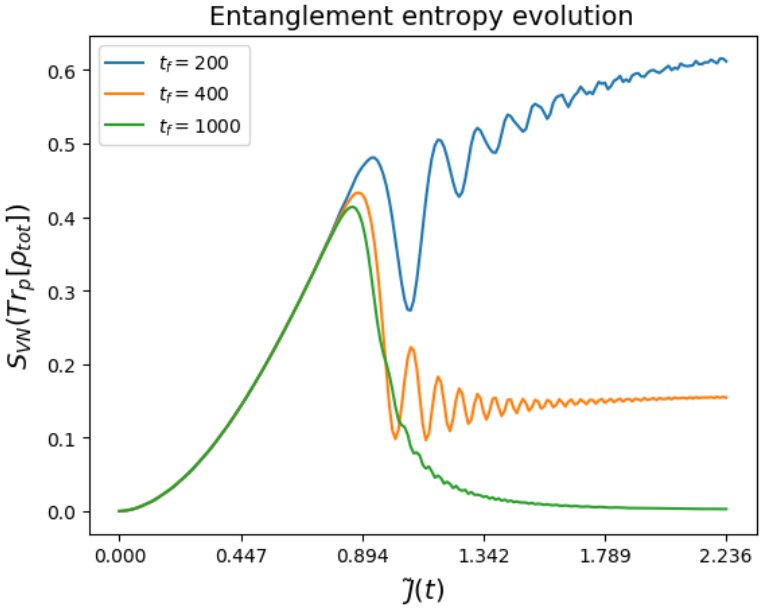

Figure 3.10: The evolution of the entanglement entropy between modes and particles is plotted. For different simulation times $t_f \in \{200, 400, 1000\}$.

the entanglement at the end of the evolution. Looking at figure 3.10 the evolution of the entropy is plotted for three different simulation times t_f. As the maximum time grows there are two things happening. First off, the entropy at the end of the simulation $t = t_f$ shrinks and eventually goes to zero. This seems already to be in agreement with the picture mentioned in Ref. [21].

As we are solving a classical optimization problem, the system needs to get rid of the entanglement such that the final field and particle states are separable and the particles assume the correct classical state, characterizing the solution. The second behavior we notice, is the build up of a single peak of maximum entanglement during the sweep. For larger t_f the maximum entropy follows the entropy of the final state until it drops below a specific peak, which will not reduce for higher evolution times. This peak is visible for all tree simulation times plotted, as it does not change significantly in height and reaches its maximum at similar evolution time. The maximum entanglement during the sweep will hence be described by this peak, for a long enough simulation time.

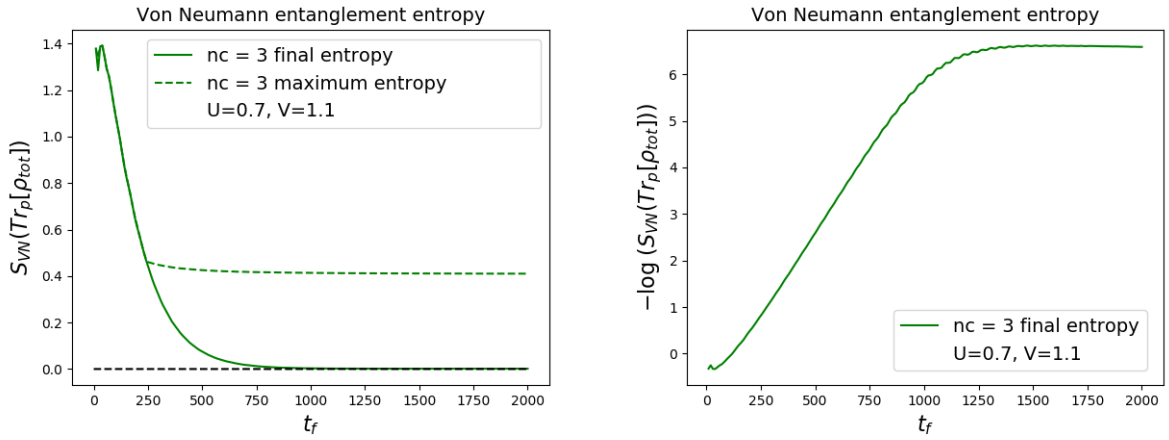

(a) (b)

Figure 3.11: Maximum entanglement entropy during an adiabatic sweep (dashed line) and the final entropy after the sweep (solid line) as a function of simulation times. The left plot shows the same on a negative logarithmic scale.

As a more systematic approach we can now look at the maximum and

final entropy generated in one sweep as a function of the simulation time t_f as we did for the fidelity. This is plotted in figure 3.11. As we can see, the results follow the behavior that we described above. The orange dotted line is the maximum entanglement. It is equal to the final entropy until we reach a simulation time where the final entropy drops below its maximum. From there it does not change significantly and keeps at a constant level. The entanglement in the final state, however, sinks continuously towards zero. This corresponds to a close to linear behavior in the negative logarithmic plot on the right side. Comparing this to the fidelity plot in figure 3.7 and 3.8 it displays a very similar evolution. This suggests that the fidelity of an adiabatic sweep depends on the ability to get rid of the entanglement for a given simulation time.

3.2 Semi-classical model and photon cut-off

In this final chapter we will discuss the most important results of this thesis. In the first part the ability for the semi-classical model to find the correct solution will be studied. In respect of this we will introduce the corresponding "phase" diagram and its connection to the system entanglement. The second part concerns somewhat interesting and unexpected behavior created by using different photon cut-offs. Specifically the improvement in simulation times for a lower cut-off.

3.2.1 Solution phase diagram and entanglement

Let us now discuss the success of the quantum annealing procedure for the semi-classical Hamiltonian (2.33). In particular, we are interested in the case where this model fails to produce the desired solution although the full quantum model succeeds. By looking at the solution fidelity of the semi-classical model for different parameters we find a very strong dependence on the particle-particle parameter U. For larger interaction we can see a sudden jump into a region, where the correct solution can not be identified any more. Looking at this result in a naive way, one can come up with a simple qualitative explanation. Since particle-particle interaction favors systems where particles are separated, increasing U inhibits the particles to occupy the same lattice site. The problem with this simple notion is that looking at the energy spectrum of the system for not too high values of U, the ground state is still the state with two particles occupying $\hat{n}_3$. Accordingly, the adiabatic sweep using the full quantum Hamiltonian (2.40) finds the correct solution also for higher U values. Continuing this naive reasoning one can also deduce that the additional well depth V should increase the probability that two particle are found in the same well, directly competing with U.

In figure 3.12 this behavior is shown in form of a phase diagram. We plot the fidelity of the final state of the adiabatic sweep using (2.33) with the correct solution state. This was done for a range of V and U parameters plotted on the y- and x- axis, respectively. One clearly sees that there are three distinct sections. The green-yellow region with high fidelity, the blue and the deep purple section.

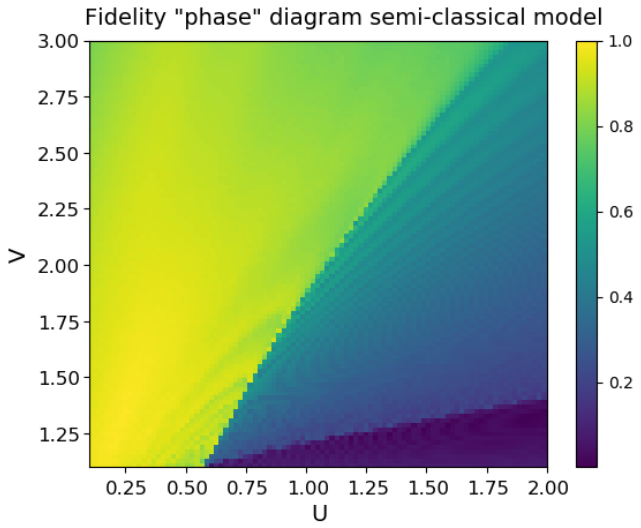

Figure 3.12: "Phase" diagram of the solution fidelity after an adiabatic sweep, using the semi-classical Hamiltonian (2.33). The parameter on the y-axis is the additional depth of the third potential well V and the x-axis is dedicated to the particle interaction strength U. Chosen parameters: $t_f = 1000$, $\Delta = -1$, $\tilde{J} = 1$, $\kappa = 1$.

To analyze this we plot the evolution of the expectation values of the site occupations $\hat{n}_{i\in\{1,2,3,4\}}$ for each region in figure 3.13. The first section in fig. 3.12 with high fidelity corresponds to the parameter range, where a correct solution to the optimization problem can be found,i.e., two particles in well three, as seen in figure 3.13 (a). In the purple region the particles organize according to the mode function $\hat{M}_1$, with a particle in well one and three (fig. 3.13 (c)). There is no probability of finding two particles in the third well, hence a zero fidelity. The middle part with non zero but low fidelity is somewhere in between. In this region there exists a probability of finding the system in the correct solution state, but it is very low. Therefore we do not consider it being successful, since most of the time we will get the wrong solution (fig. 3.13 (b)). Note that the fidelity with respect to the state that the system assumes in each region can be increased by using a slower evolution, but importantly, the simulation time will not change the structure of the diagram, i.e., the according sections will remain visible. Most surprising in 3.12 is the clear jump from finding a solution to finding no solution. There is no equivalent behavior in the "phase" diagram for the

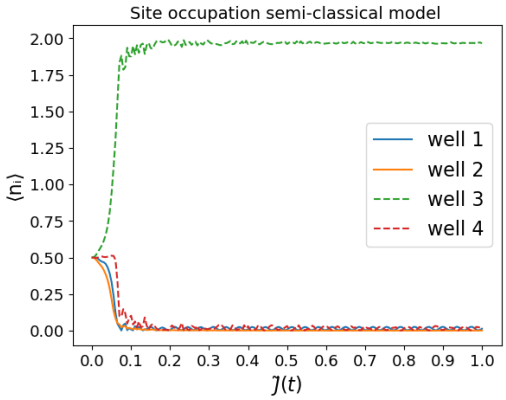

(a) Yellow region

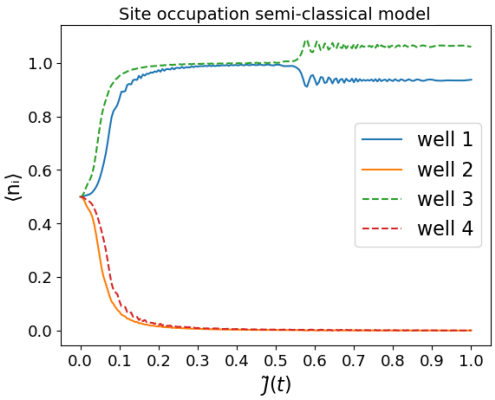

(b) Blue region

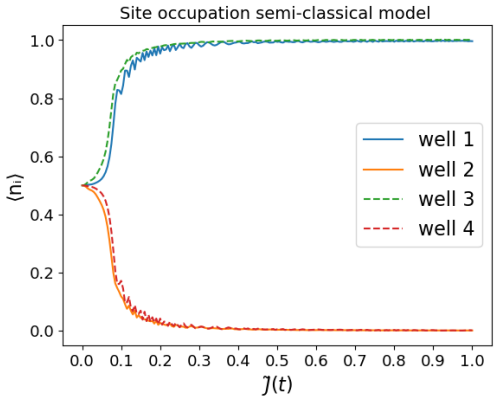

(c) Purple region

Figure 3.13: Evolution of the expectation values of the particle number operator n_i for the semi-classical model. The subplots correspond to parameters chosen from the (a) high fidelity - yellow region, (b) the blue region and (c) the purple - low fidelity region.

full quantum Hamiltonian (2.40) depicted in figure 3.14. Notice, the different scaling. The lowest points in figure (3.14) correspond to a fidelity of about $\mathcal{F} = 0.99$. Therefore, the adiabatic sweep of the full quantum Hamiltonian succeeds to find the correct solution with high probability for the whole region.

Motivated by the entanglement discussion from the previous section 3.1.3 we want to check the entanglement of the system for the parameters used in

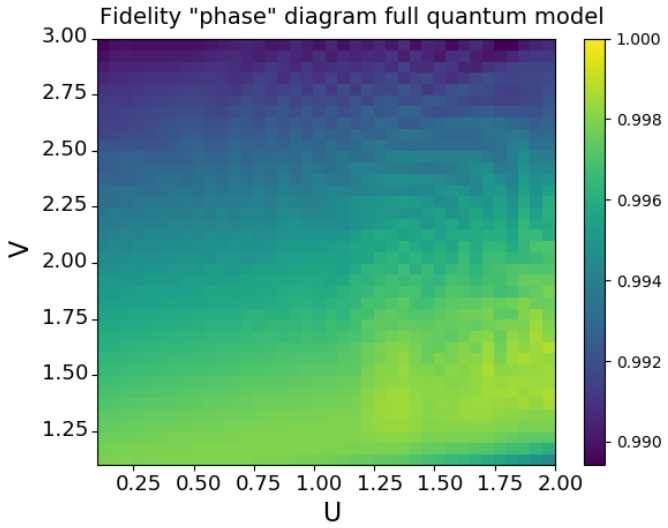

Figure 3.14: "Phase" diagram of the solution fidelity after an adiabatic sweep, using the full quantum Hamiltonian (2.40). The parameter on the y-axis is the additional depth of the third potential well V and the x-axis is dedicated to the particle interaction strength U. Chosen parameters: $t_f = 500$, $\Delta = -5$, $\tilde{J} = \sqrt{5}$.

the "phase" diagram. For that we create a figure with the same parameters, but instead of the fidelity we plot the maximum entanglement created between the modes and the particles during one sweep. In figure 3.15 the plot of the entanglement is presented together with the "phase" diagram of the semi-classical system, for comparison.

Studying the plots side by side, there seems to be a correlation between regions of high maximum entanglement and low fidelity. Especially in the right lower corner where the fidelity is close to zero we can observe a peak in the entanglement, which continues along the x-axis and reduces in intensity. One can faintly see a similar triangular behavior of the high entanglement region. Accordingly, the regions of high fidelity are accompanied by a region of low entropy, which vaguely assumes the same structure. Granted that one can easily exaggerate the similarities, especially in the high fidelity - low entropy regions, and that the boundaries are not as clear cut, the indication of a direct connection between entanglement and the success probability for the semi-classical model is convincing enough. Furthermore, as we have discussed

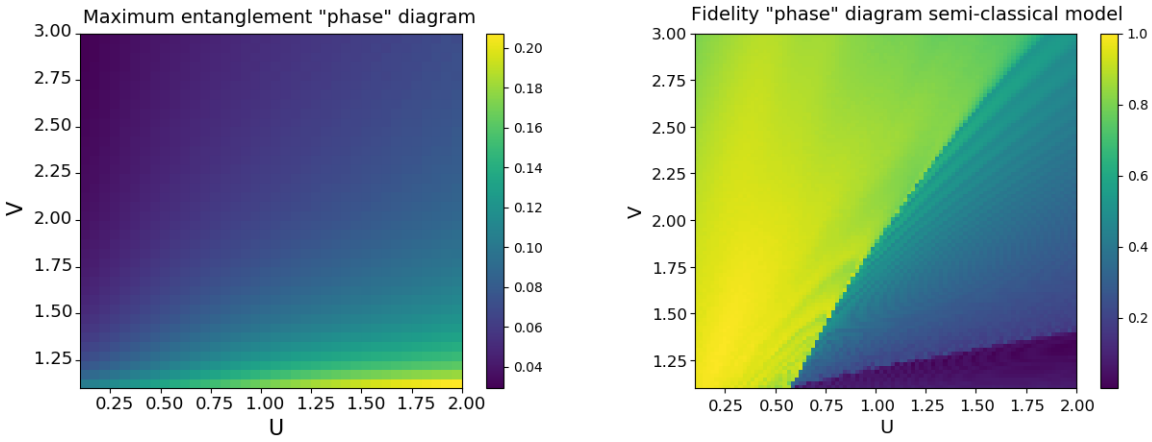

(a) Maximum entanglement

(b) Phase diagram

Figure 3.15: "Phase" diagram of (a) the maximum entanglement created during an adiabatic evolution using the full quantum Hamiltonian (2.40) and (b) the fidelity using the semi-classical model (see fig. 3.12). The parameter on the y-axis is the additional depth of the third potential well V and the x-axis is dedicated to the particle interaction strength U. Chosen parameters for plot (a): $t_f = 500$, $\Delta = -5$, $\tilde{J} = \sqrt{5}$.

previously, the approximation of classical fields is removing the ability of creating entangled particle-mode states. Hence, it is not surprising that the discrepancy between the success probabilities for the full quantum model and the semi-classical model is connected to the state entanglement. Interestingly, we can also see a clear correspondence between the entanglement peak and the reduced fidelity in the lower right corner of figure 3.14. Although, being very weak, the maximum entanglement seems to have an effect on the solution fidelity of full quantum system.

3.2.2 Photon cut-off comparison

Finally, let us compare the influence of the simulation time on the success probability for different photon cut-offs nc. We already mentioned the significance of the photon cut-off in section 3.1.2. There we argued that $nc = 3$ is an acceptable choice, reducing the numerical complexity and incorporating enough photon states to sufficiently describe the physical system. As it turns out, not every aspect of the system behaves as anticipated. Hence, we will expand the discussion and also take a closer look at lower cut-offs which reduces the quality of the numerical solution of the Schrödinger equation. Following the same arguments as before, we plot the final state occupation for cut-offs $nc \in \{1, 2, 3\}$, from left to right, in figure 3.16. It is sufficient to look at one mode, since the second does not differ significantly.

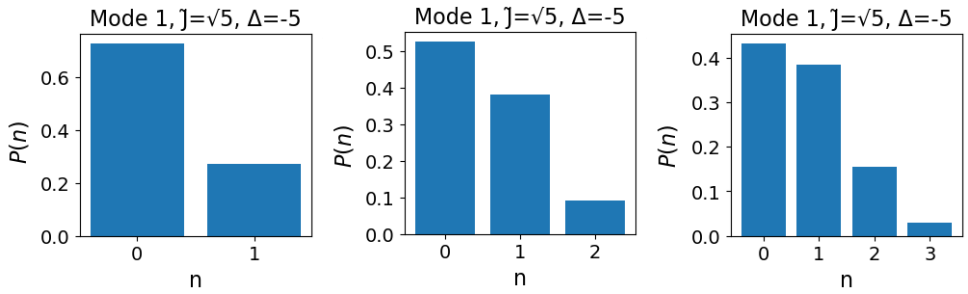

(a) $nc = 1$ (b) $nc = 2$ (c) $nc = 3$

Figure 3.16: Photon state occupation for one mode at the end of the adiabatic evolution. The plots correspond to different cut-offs: (a) $nc = 1$, (b) $nc = 2$ and (c) $nc = 3$.

Looking at the plots it becomes clearer, how strong the approximation is. Comparing the plot on the most left ($nc = 1$) and in the middle ($nc = 2$), one can see the strong effect of cutting of the $n = 2$ state. In respect to the occupation of the lower states, a probability for occupying the two photon state of about $P(n = 2) \approx 0.1$ is not insignificant. Therefore, a higher photon cut-off is desirable for faithfully simulating real world physical systems. One could then assume, that more realistic parameters are favorable in simulated quantum annealing. Surprisingly, this is not always what we found in our model. By comparing the efficiency of the system to find the correct ground state, for the chosen cut-offs, a clear advantage for lower cut-offs can be seen.

In figure 3.17 (a) the fidelity between final state of the adiabatic evolution and the correct solution state is plotted as a function of simulation time t_f and in (b) the negative logarithm of the infidelity is shown.

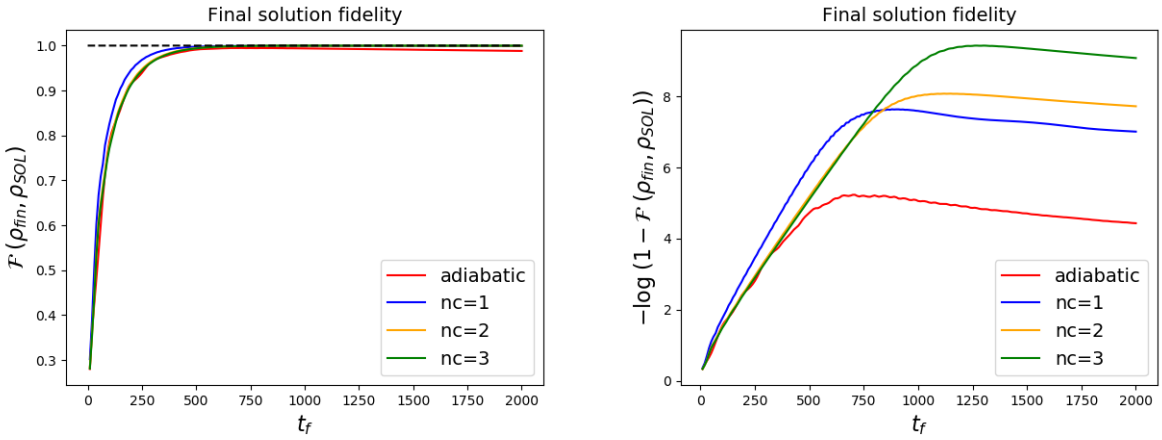

(a) Fidelity

(b) Logarithmic infidelity

Figure 3.17: (a) Fidelity between final state of the adiabatic evolution and the solution state as a function of simulation time t_f. The curves correspond to the different photon cut-offs (blue, yellow, green) and the adiabatic Hamiltonian (red). In (b) the same results are shown as the negative logarithm of the infidelity.

In the plot on the left side one can clearly see that the blue line, corresponding to $nc = 1$ cut-off, has success advantage for short simulation times. The yellow and green curves with higher cut-offs and the red one, using the adiabatic Hamiltonian (2.30), seem to be roughly equivalent. A clearer picture develops by looking at the infidelity in logarithmic scale, on the right side. While for short simulation times the same behavior is apparent, with $nc = 1$ having the most improvement and $nc = 2$ being slightly better than $nc = 3$, other interesting features appear for longer times. Focusing on the full quantum curves (blue, yellow and green) one can see that at about $t_f \approx 800$ the order changes. As the curve for the $nc = 1$ cut-off seems to reach a steady state, the yellow and green lines further improve, with the $nc = 3$ cut-off reaching its maximum at about $t_f \approx 1300$. This suggests, that considering the full quantum system and achieving an improvement on account of this, gets more relevant for longer simulation time, representing

a slower evolution but higher final fidelity. The equivalent behavior can be seen when looking at the entanglement entropy in figure 3.18. In the left plot (a) we show the Von Neumann entropy of the reduced mode state as a function of simulation time for different cut-offs. Both, the final (solid line) and the maximum entanglement (dashed line) are shown. The right plot (b) shows the same on a negative logarithmic scale.

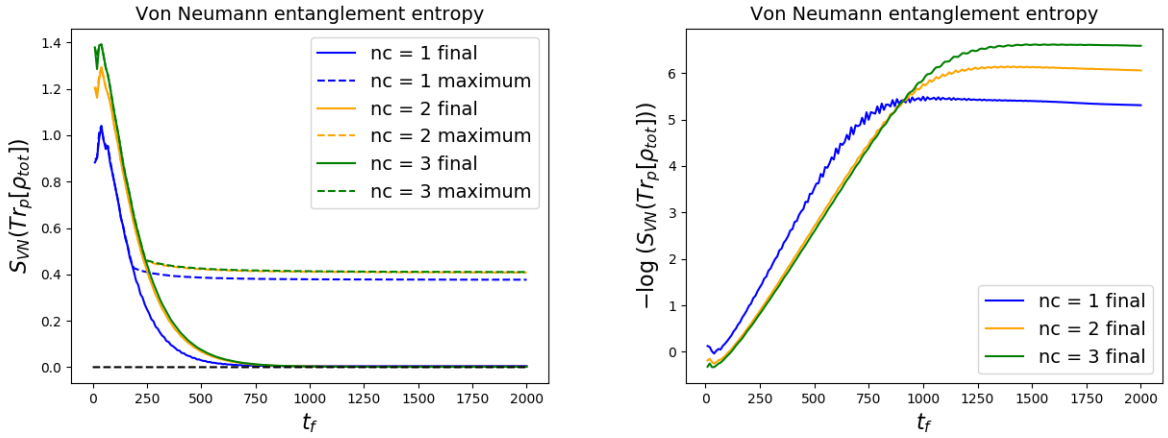

(a) Entanglement entropy

(b) Logarithmic entanglement entropy

Figure 3.18: (a) Entanglement entropy of the reduced mode sub-system as a function of simulation time t_f. Solid lines are the final entanglement of the evolution and dashed lines are the maximum entanglement generated. The curves correspond to the different photon cut-offs (blue, yellow, green). In (b) the same results are shown on a negative logarithmic scale.

We already discussed in section 3.1.3 that the entanglement at the end of an adiabatic evolution correlates with the ability to find a good solution. In figure 3.18 (a) we can see the same behavior for different photon cut-offs. Just as the fidelity for the $nc = 1$ cut-off increases the most, the entanglement reduces faster than for the other cut-offs. Also the maximum entanglement converges at a lower value. Furthermore, the curves for $nc = 2$ and $nc = 3$ are roughly equal, with the lower cut-off being slightly better. This is equivalent to the behavior of the fidelity in figure 3.17 (a). The logarithmic plot on the right side (b) reproduces the identical behavior for long simulation times. There, the lowest cut-off $nc = 1$ reaches a steady state and the highest cut-off $nc = 3$ reduces the entanglement the most.

Therefore, we again observe the indication that the final entanglement strongly correlates to the success probability, also predicting the improvements in efficiency for lower cut-offs. The same is true for the regime of long simulation times, where the more realistic cut-off can improve the quality of the solution. One can speculate that this effect might be more relevant as the system gets more complex, achieving an improvement for bigger quantum systems.

Chapter 4

Conclusions and outlook

In this thesis we have investigated the optimization technique, known as quantum annealing, for a specific Bose-Hubbard type model inside a cavity that we introduced, and compared the behavior of the full quantum model to the semi-classical approach for the cavity fields. We started by deriving a general Bose-Hubbard type cavity Hamiltonian, starting from the James Cummings model. We then applied the needed modifications to arrive at our toy model. Specifically, we assumed two atoms in a cavity, confined to an optical lattice by an external trapping potential. The atoms are then pumped directly by two transverse laser beams, scattering photons into two distinct cavity modes, generation interaction potentials. Due to periodicity we reduced the one-dimensional lattice to four lattice cites with periodic boundary conditions. We further derived the equation of an effective particle Hamiltonian by adiabatically eliminating the cavity fields. Assuming classical fields and replacing the corresponding operators by complex numbers, we construct a semi-classical Hamiltonian for our system. In the next sections we introduce the concept of quantum annealing. This is done by first considering the problems that are tackled by this method and then by explaining the basic process and its legitimization in form of the adiabatic approximation. We finally apply this model to our system and introduce a additional depth parameter for one lattice site, to lift the degeneracy in the ground state.

We proceed by giving an analysis of the full quantum model. This starts with a closer look at the energy spectrum of the system, evolving in time. We then investigate the dependence on the system parameter and briefly discuss the photon cut-off which reduces the state space to make simulations feasible. Further we look at the simulation times and connection to the

system entanglement. We find that the absence of entanglement entropy in the final state of the evolution is critical for a high success probability. In the last section we start by focusing on the semi-classical model of the system and its success ability. For that matter we present a phase diagram, dependent on the particle interaction and the additional depth parameter, which shows the region where the semi-classical model can successfully find the correct solution. Surprisingly, this is characterized by clear cut regions. In contrast to that, the full quantum model does not show this dependence. In the following we argue that these regions of no success are due to the maximum entanglement that is generated during the evolution. This is done on the basis of phase-diagram showing that the maximum entanglement peaks in these specific regions and is minimal in the successful region. We finally compare the effect of different photon cut-offs nc, where we restrict the discussion to $nc \in \{1, 2, 3\}$. Although, we argue that a higher cut-off leads to a more accurate solution of the Schrödinger equation, we observe, to our surprise, that a lower cut-off in the photon modes, allows for a higher fidelity between the sought for solution and the final evolution state. However, we see that this is more accurate for short evolution times only but not for long ones. There we can see an improvement by using a higher photon cut-off. Again, we can see a clear correlation between the final state entanglement entropy and the fidelity. Therefore, we argue that the improvement in fidelity is due to a faster decrease in the entanglement.

In essence we present a system where a clear advantage of the full quantum simulation over the semi-classical counterpart can be seen. Also we show evidence that there is a connection between maximum entanglement and the ability to find a solution by classical means. We further show a strong correlation between the solution fidelity and absence of entanglement in the final state of the evolution and can extend this argument to show that small photon cut-offs can produce better results for short simulation times. Of course, there is a lot of work which still needs to be done, to further argue for an advantage of quantum annealing and simulation in general. A deeper investigation into the entanglement of the system and its role in finding a solution is of essence. Solving the Heisenberg equations of the system operators, using a cumulant expansion, could be a promising method to uncover the entanglement dynamics. Also, an open quantum system approach with photon decay through the cavity mirrors should be considered and further studied.

Chapter 5

Appendix

5.1 Program example

Here we include a Julia code example for calculating the time evolution, energy spectrum and finally the fidelity and entanglement as a function of simulation time. We used the quantum optics toolbox QuantumOptics.jl [31] version 0.8.2 and Julia version 1.5.1.

Definitions. In the following we first introduce all the needed definitions.

```
using QuantumOptics # quantum optics toolbox
using PyPlot        # Plot generation
using LinearAlgebra # linear algebra functions

# System setup / Hilbertspace dimensions
N=2;    # particle number / Well Fock space
nc=1;   # photon cutoff / Photon Fock space
dim=(N+1)^4*(nc+1)^2 # Full dimension of model

# Physical parameters
κ=1.            # cavity loss rate
Δ=-1*κ *5       # laser-cavity detuning
U=0.7*κ         # particle-particle on site interaction
J=0.1*κ         # hopping strength
J̃ =1*κ* sqrt(5)  # pump strength
```

```
V=1.1           # pertubation of 3rd well


#Particle and Photon basis
# 4 potential wells, 2 modes,  Periodic boundary conditions 1-2-3-4-1
#   1. mode - + - +
#   2. mode + + - -

basisp=FockBasis(N);    basispN=basisp^4;
basisf=FockBasis(nc); basisfnc=basisf^2;
basisPF=basispN⊗basisfnc;

# cavity field operators
a(n) = embed(basisPF,n+4,destroy(basisf));
ad(n)=dagger(a(n));
nph(n)=ad(n)*a(n);

# Particle creation and annihilator operators
b=Any[];
[push!(b,embed(basisPF,i,destroy(basisp))) for i in 1:4]
bd=dagger.(b);
n=[bd[i]*b[i] for i in 1:4];

# Tunnel Hamiltonian - Jump Operator
j_op=(b[1]*bd[2]+b[2]*bd[3]+b[3]*bd[4]+b[4]*bd[1] +
    dagger(b[1]*bd[2]+b[2]*bd[3]+b[3]*bd[4]+b[4]*bd[1]));

# System Mode Operators
M1=(-n[1] + n[2] - V * n[3] + n[4]) # - + - +
M2=( n[1] + n[2] - V * n[3] - n[4]) # + + - -

# Adiabatic eliminated field operators
a1=-1im*J̃/(κ-1im*Δ)*M1; n1=dagger(a1)*a1
a2=-1im*J̃/(κ-1im*Δ)*M2; n2=dagger(a2)*a2

# System Hamiltonians
H_tun = J * j_op;                       # Tunneling Hamiltonian
H_rad = -Δ*(ad(1)*a(1)+ad(2)*a(2));     # Cavity field Hamiltonian
```

```
U_int = U/2 * (sum(n.^2-n));            # On-site interaction Hamiltonian
H_int = J̃*(M1*(a(1)+ad(1))+M2*(a(2)+ad(2))) # Field - particle interaction Hamiltonian

H_ad=Δ/(κ^2+Δ^2)*(M1^2+M2^2)          # Adiabatic eliminated Hamiltonian

# Semi- classical Hamiltonian
H_ad_cl(t,psi)=Δ/(κ^2+Δ^2)*((2*M1*expect(M1,psi)-
        identityoperator(basisPF)*expect(M1,psi)^2)
        +(2*M2*expect(M2,psi)-
        identityoperator(basisPF)*expect(M2,psi)^2))


# Annealing shedule ramp up time
tmax=1000; dt=tmax/200; t=[0.:dt:tmax;] # max. sim. time / timesteps / time range
δt(t)=(t/tmax); # timedependant ramp

# Full Hamiltonians
Hf(t,psi)=H_tun +  U_int + H_rad + δt(t) * H_int;        # Full Quantum Hamiltonian
Had(t,psi)=H_tun + U_int + δt(t) * J̃^2 * H_ad;           # Adiabatically eliminated Ham.
Hcl(t,psi)=H_tun + U_int + δt(t) * J̃^2 * H_ad_cl(t,psi); # Semi- calssical Ham.

#
# State declarations
#

vac=basisstate(basisPF,1)                                    # Vacuum state
SF = 1/sqrt(2)*((bd[1]-bd[2]+bd[3]-bd[4])/sqrt(4))^2*vac;     # Superfluid state
MI1 = 1/sqrt(2)*(bd[1]*bd[1])*vac;                           # 2 particles in 1st well
MI2 = 1/sqrt(2)*(bd[2]*bd[2])*vac;                           # 2 particles in 2nd well
MI3 = 1/sqrt(2)*(bd[3]*bd[3])*vac;                           # 2 particles in 3rd well
MI4 = 1/sqrt(2)*(bd[4]*bd[4])*vac;                           # 2 particles in 4th well


# Starting eigenstate identification /
# Identify lowest eigenstate with 2 particles for t=0

ψ0=eigenstates(dense(H_tun + U_int + H_rad))[2];
for i in 1:length(eigenstates(dense(H_tun + U_int + H_rad))[2])
```

```
    global ψ0
    if round(real(expect(sum(n),ψ0[i])))==2
        ψ0=eigenstates(dense(H_tun + U_int + H_rad))[2][i];
        break
    end
end

# Final solution eigenstate identification /
# Identify lowest eigenstate with 2 particles for t=tmax

ψfin=eigenstates(dense(Hf(t[end],0)))[2];
for i in 1:length(eigenstates(dense(Hf(t[end],0)))[2])
    global ψfin
    if round(real(expect(sum(n),ψfin[i])))==2
        ψfin=eigenstates(dense(Hf(t[end],0)))[2][i];
        break
    end
end
```

Energy spectrum. We can calculate and plot the energy levels as in figure 3.1. Note that we have to select the two particle states explicitly, as the eigenstates of the Hamiltonian are not restricted to two particles.

```
#
#    Energy Spectrum
#
#    Calculation of the Energyspectrum for two particle states

lvl=2  # determines how many energylevels are calculated ( including ground state)

Et=zeros(Float64,200,lvl);
for ti in 1:200
    ψe = eigenstates(dense(Hf(t[ti+1],0)))[2];
    j=1
    for i in 1:length(eigenstates(dense(Hf(t[1],0)))[2])
        if round(real(expect(sum(n),ψe[i]))) == 2  # only use two particle states.
            e=eigenstates(dense(Hf(t[ti+1],0)))[1][i];
            Et[ti,j] = e;
```

```
            j+=1
            if j == lvl+1
                break
            end
        end
    end
end

Δmin=minimum((Et[:,2] - Et[:,1])) # minimum energy gap of ground and excited state

# Energyspectrum Plot, resecaling relative to ground state energy
E0=Et[:,1]
figure(figsize=(12,4))
[plot([J̃/200:J̃/200:J̃;],Et[:,i]-E0) for i in 1:lvl]
vlines(argmin(Et[:,2] - Et[:,1])*J̃/200,0,Δmin,label="Δmin ≈ $Δmin",
    "black","dotted",linewidth=2)
xlim(0.0,sqrt(5));ylim(-0.1,2);
ylabel(L"E_n(t)-E_0",size=14);xlabel(L"J̃ ",size=14);
title("Energy spectrum as a function of pump strength J̃ ")
legend(fontsize=14);
```

Schrödinger time-evolution. The following code computes the time evolution of the given Hamiltonian with initial state ψ_0 using the Schrödinger equation. We can then plot the expectation values of the lattice site occupation numbers and the state fidelity (fig. 3.9).

```
#
# Schrödinger timeevolutions for given time and Hamiltonian
#

tf,ψf_sg = timeevolution.schroedinger_dynamic(t,ψ0,Hf);
tad,ψad_sg = timeevolution.schroedinger_dynamic(t,ψ0,Had);
tcl,ψcl_sg = timeevolution.schroedinger_dynamic(t,ψ0,Hcl);

#
#   Plot of the full Quantum Hamiltonian (Hf) evolution
#   with site occupation and state fidelities
```

```
time = [0:J̃/200:J̃;]
figure(figsize=(12,4))
subplot(1,2,1)
plot(time,expect(n[1],ψf_sg),label="well 1",linestyle="-")
plot(time,expect(n[2],ψf_sg),label="well 2",linestyle="-")
plot(time,expect(n[3],ψf_sg),label="well 3",linestyle="-")
plot(time,expect(n[4],ψf_sg),label="well 4",linestyle="-")
ylabel("⟨nᵢ⟩",size=14);legend(fontsize=11);
title("Particle Position Semi-Classical Hamiltonian",size=12);
xticks([0:1/sqrt(J̃):sqrt(J̃);],size=12);
xlabel(L" J̃(t) ",size=16);

subplot(1,2,2)
plot(time,[fidelity(ptrace(ψfin,[5,6]),ptrace(ψf_sg[i],[5,6]))
        for i in 1:201],label="Final particle state fidelity");
plot(time,[fidelity(ptrace(ψfin,[1,2,3,4]),ptrace(ψf_sg[i],[1,2,3,4]))
        for i in 1:201],label="Final mode state fidelity");
plot(time,[fidelity(ptrace(ψ0,[5,6]),ptrace(ψf_sg[i],[5,6]))
        for i in 1:201],label="Initial state fidelity");
plot(time,[fidelity(ptrace(MI3,[5,6]),ptrace(ψf_sg[i],[5,6]))
        for i in 1:201], label="Well 3 two particles","--");
plot(time,ones(201),"black",linestyle="--");
xticks([0:1/sqrt(J̃):sqrt(J̃);],size=12);
xlabel(L" J̃(t) ",size=16);ylabel(L"\mathcal{F}\;(ρ_{end},ρ_{sol})",size=16);
title("Fidelity final states",size=12);legend(fontsize=10);
```

Fidelity and entanglement. Finally, we solve the Schrödinger equation for different simulation times and plot the final entanglement, maximum entanglement and the fidelity between the final state and the correct target state, shown in figure 3.7 and 3.11.

```
#
#   Solving the Schrödinger equation for different simulation times
#

maxtf=100 # maximum sim. time

ψf_t=[]   # states of the full quantum model
```

```
ψad_t=[]  # states of the adiabatic model

for i in 1:maxtf
    tmax=i*10; dt=tmax/200;   t=[0.:dt:tmax;]
    δt(t)=(t/tmax); # timedependant ramp
    Hf(t,psi)=H_tun +  U_int + H_rad + δt(t) * H_int;
    Had(t,psi)=H_tun + U_int + δt(t) * J̃^2 * H_ad;

    tf,ψf_sg=timeevolution.schroedinger_dynamic(t,ψ0,Hf);
    tad,ψad_sg=timeevolution.schroedinger_dynamic(t,ψ0,Had);

    push!(ψf_t,ψf_sg); push!(ψad_t,ψad_sg);
end



# calculating and plotting the entanglement and fidelity
# as a function of simulation time

ent_f=[]; ent_max=[];
fidf=[]; fidad=[];

for j in 1:maxtf
    push!(ent_f,abs(entropy_vn(
          ptrace(ψf_t[j][end] ⊗ dagger(ψf_t[j][end]), [1,2,3,4]))))
    push!(ent_max,maximum([abs(entropy_vn(
          ptrace(ψf_t[j][i] ⊗ dagger(ψf_t[j][i]), [1,2,3,4])))
          for i in 1:length(ψf_t[j])]))
    push!(fidf,fidelity(ptrace(ψfin,[5,6]),ptrace(ψf_t[j][end],[5,6])))
    push!(fidad,fidelity(ptrace(ψfin,[5,6]),ptrace(ψad_t[j][end],[5,6])))
end

figure()
plot([1:maxtf;] .*10, ent_f,label="nc = $nc final entropy",linestyle="-")
plot([1:maxtf;] .*10,ent_max,label="nc = $nc maximum entropy",linestyle="--")
plot(zeros(maxtf*10),"black",linestyle="--");
title("Von Neumann entanglement entropy",size=14);
ylabel(L" S_{VN}(Tr_{p}[ρ_{tot}])",size=16); xlabel(L"t_f",size=16);
```

```
legend(fontsize=14);

figure()
plot([1:1:maxtf;] .*10, abs.(fidad),label="adiabatic Hamiltonian")
plot([1:1:maxtf;] .*10, abs.(fidf),label="full quantum Hamiltonian")
plot(ones(maxtf*10),"black",linestyle="--");
title("Final solution fidelity",size="14");
ylabel(L" \mathcal{F}\;(ρ_{fin},ρ_{SOL})",size=16); xlabel(L"t_f",size="16");
legend(fontsize="14");
```

Bibliography

[1] T. Albash and D. A. Lidar. Demonstration of a scaling advantage for a quantum annealer over simulated annealing. *Phys. Rev. X*, 8:031016, Jul 2018.

[2] B. Apolloni, C. Carvalho, and D. de Falco. Quantum stochastic optimization. *Stochastic Processes and their Applications*, 33(2):233 – 244, 1989.

[3] B. Apolloni, N. Cesa-Bianchi, and D. de Falco. A numerical implementation of "quantum annealing". In *Stochastic processes, physics and geometry (Ascona and Locarno, 1988)*, pages 97–111. World Sci. Publ., Teaneck, NJ, 1990.

[4] J. Asbóth, P. Domokos, H. Ritsch, and A. Vukics. Self-organization of atoms in a cavity field: Threshold, bistability, and scaling laws. *Physical Review A*, 72, 09 2005.

[5] R. Babbush, P. J. Love, and A. Aspuru-Guzik. Adiabatic quantum simulation of quantum chemistry. *Scientific Reports*, 4(1), Oct 2014.

[6] P. Benioff. The computer as a physical system: A microscopic quantum mechanical hamiltonian model of computers as represented by turing machines. *Journal of Statistical Physics*, 22:563–591, 05 1980.

[7] M. Born and V. Fock. Beweis des Adiabatensatzes. *Zeitschrift fur Physik*, 51(3-4):165–180, Mar. 1928.

[8] M. Born and V. Fock. Beweis des Adiabatensatzes. *Zeitschrift fur Physik*, 51(3-4):165–180, Mar. 1928.

[9] H. Breuer, P. Breuer, F. Petruccione, and S. Petruccione. *The Theory of Open Quantum Systems*. Oxford University Press, 2002.

[10] J. W. Britton, B. C. Sawyer, A. C. Keith, C.-C. J. Wang, J. K. Freericks, H. Uys, M. J. Biercuk, and J. J. Bollinger. Engineered two-dimensional ising interactions in a trapped-ion quantum simulator with hundreds of spins. *Nature*, 484(7395):489–492, Apr 2012.

[11] P. I. Bunyk, E. M. Hoskinson, M. W. Johnson, E. Tolkacheva, F. Altomare, A. J. Berkley, R. Harris, J. P. Hilton, T. Lanting, A. J. Przybysz, and et al. Architectural considerations in the design of a superconducting quantum annealing processor. *IEEE Transactions on Applied Superconductivity*, 24(4):1–10, Aug 2014.

[12] D. Deutsch. Quantum theory, the Church-Turing principle and the universal quantum computer. *Proceedings of the Royal Society of London Series A*, 400(1818):97–117, July 1985.

[13] R. H. Dicke. Coherence in spontaneous radiation processes. *Phys. Rev.*, 93:99–110, Jan 1954.

[14] P. Domokos and H. Ritsch. Mechanical effects of light in optical resonators. *JOSA B*, 20, 05 2003.

[15] J. P. Dowling and G. J. Milburn. Quantum technology: The second quantum revolution, 2002.

[16] S. F. Edwards and P. W. Anderson. Theory of spin glasses. *Journal of Physics F Metal Physics*, 5(5):965–974, May 1975.

[17] H. Feshbach. Quantum mechanics. vol. 1. albert messiah. translated by g. m. temmer. north-holland, amsterdam; interscience, new york, 1961. xv + 504 pp. illus. 15. *Science*, 136(3515):514–514, 1962.

[18] R. P. Feynman. Simulating Physics with Computers. *International Journal of Theoretical Physics*, 21(6-7):467–488, June 1982.

[19] R. Grimm, M. Weidemüller, and Y. B. Ovchinnikov. Optical dipole traps for neutral atoms, 1999.

[20] P. Hauke, L. Bonnes, M. Heyl, and W. Lechner. Probing entanglement in adiabatic quantum optimization with trapped ions. *Frontiers in Physics*, 3:21, 2015.

[21] P. Hauke, H. G. Katzgraber, W. Lechner, H. Nishimori, and W. D. Oliver. Perspectives of quantum annealing: methods and implementations. *Reports on Progress in Physics*, 83(5):054401, May 2020.

[22] K. Huang. *Statistical Mechanics*. Wiley, 1987.

[23] D. Jaksch, C. Bruder, J. I. Cirac, C. W. Gardiner, and P. Zoller. Cold bosonic atoms in optical lattices. *Phys. Rev. Lett.*, 81:3108–3111, Oct 1998.

[24] E. T. Jaynes and F. W. Cummings. Comparison of quantum and semiclassical radiation theories with application to the beam maser. *Proceedings of the IEEE*, 51(1):89–109, 1963.

[25] M. Johnson, M. Amin, S. Gildert, T. Lanting, F. Hamze, N. Dickson, R. Harris, A. Berkley, J. Johansson, P. Bunyk, E. Chapple, C. Enderud, J. Hilton, K. Karimi, E. Ladizinsky, N. Ladizinsky, T. Oh, I. Perminov, C. Rich, M. Thom, E. Tolkacheva, C. Truncik, S. Uchaikin, J. Wang, B. Wilson, and G. Rose. Quantum annealing with manufactured spins. *Nature*, 473(7346):194–198, May 2011.

[26] R. Johnson and M. G. Pilcher. The traveling salesman problem, edited by e. l. lawler, j. k. lenstra, a.h.g. rinnooy kan, and d.b. shmoys, john wiley & sons, chichester, 1985, 463 pp. *Networks*, 19(5):615–616, 1989.

[27] G. Jotzu, M. Messer, R. Desbuquois, M. Lebrat, T. Uehlinger, D. Greif, and T. Esslinger. Experimental realization of the topological haldane model with ultracold fermions. *Nature*, 515(7526):237–240, Nov 2014.

[28] T. Kadowaki. Study of optimization problems by quantum annealing, 2002.

[29] T. Kato. On the adiabatic theorem of quantum mechanics. *Journal of the Physical Society of Japan*, 5(6):435–439, 1950.

[30] C. Kittel. *Quantum Theory of Solids*. Wiley, 1987.

[31] S. Krämer, D. Plankensteiner, L. Ostermann, and H. Ritsch. Quantumoptics. jl: A julia framework for simulating open quantum systems. *Computer Physics Communications*, 227:109–116, 2018.

[32] C. Letavec and J. Ruggiero. The n-queens problem. *INFORMS Transactions on Education*, 2(3):101–103, 2002.

[33] M. Lewenstein, A. Sanpera, and V. Ahufinger. Ultracold atoms in optical lattices: Simulating quantum many-body systems. 01 2012.

[34] S. Lloyd, M. Mohseni, and P. Rebentrost. Quantum algorithms for supervised and unsupervised machine learning, 2013.

[35] A. Lucas. Ising formulations of many np problems. *Frontiers in Physics*, 2:5, 2014.

[36] K.-P. Marzlin and B. C. Sanders. Inconsistency in the application of the adiabatic theorem. *Phys. Rev. Lett.*, 93:160408, Oct 2004.

[37] C. Maschler, I. B. Mekhov, and H. Ritsch. Ultracold atoms in optical lattices generated by quantized light fields. *The European Physical Journal D*, 46(3):545–560, Feb 2008.

[38] A. Perdomo-Ortiz, N. Dickson, M. Drew-Brook, G. Rose, and A. Aspuru-Guzik. Finding low-energy conformations of lattice protein models by quantum annealing, 2012.

[39] J. Preskill. Quantum Computing in the NISQ era and beyond. *Quantum*, 2:79, Aug. 2018.

[40] H. Ritsch, P. Domokos, F. Brennecke, and T. Esslinger. Cold atoms in cavity-generated dynamical optical potentials. *Rev. Mod. Phys.*, 85:553–601, Apr 2013.

[41] J. Sakurai. *Advanced Quantum Mechanics*. Always learning. Pearson Education, Incorporated, 1967.

[42] V. Torggler, P. Aumann, H. Ritsch, and W. Lechner. A quantum n-queens solver. *Quantum*, 3:149, Jun 2019.